Review article **Open Access**

Shawn Sederberg, Curtis J. Firby, Shawn R. Greig and Abdulhakem Y. Elezzabi*

Integrated nanoplasmonic waveguides for magnetic, nonlinear, and strong-field devices

DOI 10.1515/nanoph-2016-0135
Received August 2, 2016; revised September 23, 2016; accepted October 2, 2016

Abstract: As modern complementary-metal-oxide-semiconductor (CMOS) circuitry rapidly approaches fundamental speed and bandwidth limitations, optical platforms have become promising candidates to circumvent these limits and facilitate massive increases in computational power. To compete with high density CMOS circuitry, optical technology within the plasmonic regime is desirable, because of the sub-diffraction limited confinement of electromagnetic energy, large optical bandwidth, and ultrafast processing capabilities. As such, nanoplasmonic waveguides act as nanoscale conduits for optical signals, thereby forming the backbone of such a platform. In recent years, significant research interest has developed to uncover the fundamental physics governing phenomena occurring within nanoplasmonic waveguides, and to implement unique optical devices. In doing so, a wide variety of material properties have been exploited. CMOS-compatible materials facilitate passive plasmonic routing devices for directing the confined radiation. Magnetic materials facilitate time-reversal symmetry breaking, aiding in the development of nonreciprocal isolators or modulators. Additionally, strong confinement and enhancement of electric fields within such waveguides require the use of materials with high nonlinear coefficients to achieve increased nonlinear optical phenomenon in a nanoscale footprint. Furthermore, this enhancement and confinement of the fields facilitate the study of strong-field effects within the solid-state environment of the waveguide. Here, we review current state-of-the-art physics and applications of nanoplasmonic waveguides pertaining to passive, magnetoplasmonic, nonlinear, and strong-field devices. Such components are essential elements in integrated optical circuitry, and each fulfill specific roles in truly developing a chip-scale plasmonic computing architecture.

Keywords: nanoplasmonics; waveguides; integrated optics; ultrafast optics; nonlinear optics; magnetoplasmonics; strong field phenomena.

1 Introduction

Fiber-optical networks provide tremendous advantages in terms of transmission bandwidth and propagation loss compared with their electrical predecessors. As a result, optical data transmission systems are increasingly replacing their electrical counterparts. This superiority extends down to the chip-scale, which has motivated intensive research efforts by semiconductor corporations to replace long copper electrical interconnects with silicon (Si) photonic waveguides on computer processors [1]. The bandwidth bottleneck created by electrical signal transmission can be gradually alleviated as lossless optical systems continue to replace electrical systems. As this integration between electrical and optical systems grows, it will be necessary for optical systems to interface with electronic circuitry of decreasing dimensions, increasing density, and increasingly complex functionality. This is a primary source of motivation for research into a multitude of nanophotonic and nanoplasmonic waveguide devices operating on a wide range of physical principles.

High-index contrast Si photonic waveguides, depicted schematically in Figure 1(A), enable the reduction of the waveguide cross-sectional dimensions to the scale of 200 nm–300 nm at $\lambda = 1550$ nm. Based on their high refractive index, low loss in the telecommunications band, and complementary-metal-oxide-semiconductor (CMOS)-compatible material platform, Si photonic waveguides have received the most extensive research efforts. However, their ability to address the smallest electronic devices, on the order of 10 nm, is fundamentally limited by the light wave diffraction limit. As the Si core dimensions

***Corresponding author: Abdulhakem Y. Elezzabi,** University of Alberta, Ultrafast Optics and Nanophotonics Research Laboratory, Edmonton, Alberta T6G 2V4, Canada,
e-mail: elezzabi@ece.ualberta.ca
Shawn Sederberg, Curtis J. Firby and Shawn R. Greig: University of Alberta, Ultrafast Optics and Nanophotonics Research Laboratory, Edmonton, Alberta T6G 2V4, Canada

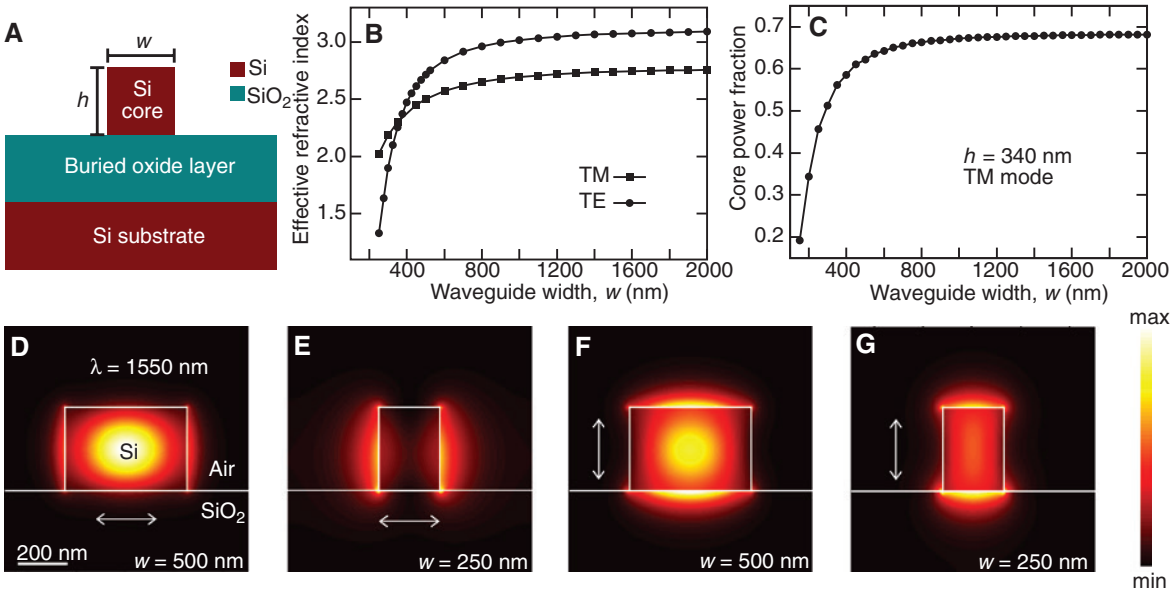

Figure 1: Electromagnetic confinement in Si photonic waveguides. (A) Schematic depiction of a Si photonic waveguide. (B) Effective refractive index of the quasi-TE and quasi-TM waveguide modes for a fixed waveguide height, $h = 340$ nm, and varying waveguide width, w. (C) Fraction of the quasi-TM mode energy that is confined to the Si waveguide core as a function of waveguide width, w. (D) Quasi-TE mode profile, $w = 500$ nm. (E) Quasi-TE mode profile, $w = 250$ nm. (f) Quasi-TM mode profile, $w = 500$ nm. (G) Quasi-TM mode profile, $w = 250$ nm.

are reduced further and further, electromagnetic energy can no longer be fully confined to the waveguide core and a significant fraction of the mode propagates in the surrounding materials. This is highlighted in Figure 1(B)–(C), which illustrate the effective refractive index of the quasi-transverse-electric (quasi-TE) and quasi-transverse-magnetic (quasi-TM) waveguide modes, as well as the fraction of electromagnetic energy confined to the Si waveguide core for a constant waveguide height, $h = 340$ nm, and varying waveguide width, w. As w is reduced to less than approximately 600 nm, the waveguide mode confinement reduces rapidly. Figure 1(D)–(G) graphically depict the quasi-TE and quasi-TM mode profiles for Si photonic waveguides with two different widths, namely, $w = 500$ nm and $w = 250$ nm. Evidently, more of the mode propagates outside of the Si core as w is decreased. As a result, cross-talk between adjacent waveguides becomes increasingly problematic, and nonlinear optical interactions in the Si core are reduced. Both of these issues hinder the performance of high-density nonlinear optical circuitry.

Meanwhile, nanoplasmonic waveguides have the attractive ability to confine and enhance electric fields to the vicinity of their constituent nanometallic surfaces, enabling passive and active functionalities at deeply subwavelength dimensions. These nanoscale metallic features strongly couple the electric fields of the propagating waveguide mode to the metal's free electrons, in a form of a quasi-particle called a surface plasmon polariton (SPP) [2]. Such a strong coupling enables confinement to dimensions, which are significantly smaller than the free-space wavelength of the propagating light signals. The geometry and mode profile for a nanoplasmonic slot waveguide are illustrated in Figure 2(A)–(B). Notably, the electromagnetic fields are tightly confined to the Au interfaces, and even for core widths of $w = 100$ nm, the mode is almost entirely within the Si core. Tighter confinement, arising from more intimate interaction with metals, gives rise to higher optical losses. In general, there exists a trade-off between nanoplasmonic mode confinement and its propagation losses, which is illustrated in Figure 2(C). As w is decreased, the electromagnetic fields are confined more tightly to the Au-Si interfaces, thus giving rise to a higher effective refractive index and higher losses. However, in contrast to Si photonic waveguides, as the core width of the nanoplasmonic slot waveguide is decreased, the waveguide confines electromagnetic energy even better, as shown in Figure 2(D). Although this geometry is commonly used for research purposes, the horizontal orientation of the geometry makes its direct implementation in practical devices quite challenging.

Ideally, emerging chip-scale technologies would enable monolithic integration of electronic, photonic, and nanoplasmonic waveguide devices [3–9]. In such a scheme, electronic devices would continue to perform their typical functionality, photonic waveguides would be used for low-loss, high-bandwidth signal transmission

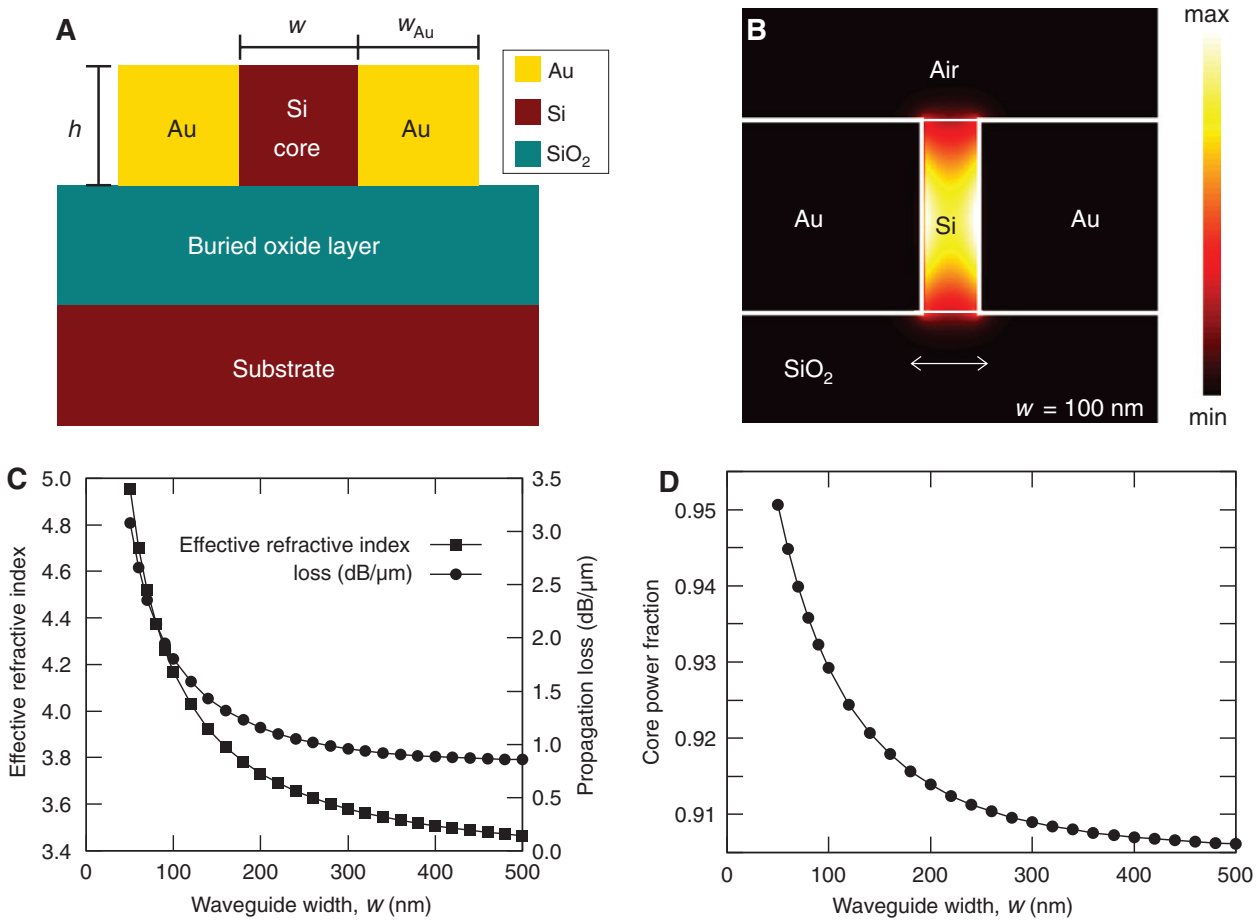

Figure 2: Nanoplasmonic slot waveguides. (A) Schematic depiction of a slot waveguide with Au-Si-Au layers. (B) Mode profile of a Au-Si-Au waveguide with $w = 100$ nm. (C) Effective refractive index and propagation losses of the Au-Si-Au waveguide mode for a fixed waveguide height, $w = 340$ nm and varying width, w. (D) Fraction of the mode energy that is confined to the Si core as a function of waveguide width, w.

and multiplexing/demultiplexing of narrowband signals, and nanoplasmonic waveguides would be used for bridging the dimensional gap between photonic and electronic devices, high-density optical circuitry, as well as efficient nonlinear and magnetoplasmonic devices. With this integrated device architecture, developing nanoplasmonic waveguide devices based on materials and fabrication processes, which are compatible with electronic and photonic technologies, become desirable.

The extraordinary properties of nanoplasmonic devices have motivated significant efforts in several fields of research [10], including sensing [11], light-matter interaction enhancement [12–23], light amplification [24–31], sub-diffraction imaging [32], metamaterials [33, 34], and planar optical circuitry [35, 36]. In this Review, we will focus exclusively on the use of nanoplasmonic waveguides in planar optical circuitry and on related developments of integrated devices with advanced functionalities. Specifically, we provide an overview of research developments related to passive routing, magnetoplasmonics, nonlinear optics and signal modulation, as well as strong field interactions in nanoplasmonic waveguides.

2 Passive routing

Typical nanoplasmonic waveguide geometries consist of one or two metal films combined with one or more dielectric slabs. Common metals used in nanoplasmonic waveguides are gold (Au), silver (Ag), copper (Cu), and aluminum (Al). More recently, transparent conductive oxides and other exotic materials have been proposed as plasmonic materials for near- to mid-infrared signals [37–39]. The choice of dielectric materials that are used to load the nanoplasmonic waveguides depends largely on the intended function of the nanoplasmonic waveguide. Practically, it is desirable to conform to materials that are commonly used in the electronics and photonics

industries, such as Si, silicon nitride (Si_3N_4), and silicon dioxide (SiO_2). In general, low-index materials enable longer propagation lengths, but provide lower confinement. Waveguides intended for nonlinear optical interactions should include dielectrics exhibiting high nonlinear optical coefficients, such as Si, Si_3N_4, or organic polymers. Waveguides designed for magneto-optical interactions must incorporate dielectrics with high magneto-optical coefficients, such as rare earth iron garnet, or ferromagnetic metals, such as iron (Fe), nickel (Ni), or cobalt (Co).

Several figures of merit (FoM) can be used to quantify the spatial confinement provided by a nanoplasmonic waveguide design [40, 41]. The first is based on the dimensions of the waveguide mode and, for a one-dimensional waveguide, can be defined as

$$M_1^{1D} = \frac{1}{\delta_w \alpha_z}, \tag{1}$$

where δ_w represents the spatial separation between the $1/e$ points of the primary transverse electric field and α_z is the attenuation constant of the waveguide mode. A similar FoM can be constructed for two-dimensional (2D) geometries

$$M_1^{2D} = \sqrt{\frac{\pi}{A_e}} \frac{1}{\alpha_z}, \tag{2}$$

where A_e is the area contained by the contour enclosing the $1/e$ field roll-off. An alternative FoM relates to the deviation of the effective refractive index of the waveguide, n_{eff}, from that of the dielectric, n_1, and is expressed as

$$M_2 = (n_{\text{eff}} - n_1)/\alpha_z. \tag{3}$$

A third FoM is based on the inverse effective wavelength of the waveguide mode and is given by

$$M_3 = 1/\lambda_g \alpha_z, \tag{4}$$

where λ_g is the effective wavelength of the waveguide mode. Each FoM provides a slightly different approach to assessing the waveguide mode confinement. Therefore, careful consideration must be given to the physical meaning of each FoM when evaluating waveguide designs.

Early demonstrations of signal routing in plasmonic waveguide systems were based on long-range SPPs (LRSPP), where thin metal stripes with a 8 μm width and 20 nm thickness were demonstrated in the routing of $\lambda = 1550$ nm signals over lengthscales exceeding 8 mm [42, 43]. Since then, extensive works have focused on low-loss signal routing in waveguide structures that confine the radiation to deeply subwavelength dimensions. Several pioneering investigations utilized metallic wedges or triangular channels as plasmonic waveguides, as shown in Figure 3(A)–(B), where the triangular features enabled field confinement and signal routing at subwavelength dimensions [44–47]. Although interesting from the scientific and developmental perspectives, such three-dimensional (3D) structures are generally avoided in electronic and photonic circuitry, and subsequent advances have focused on nanoplasmonic waveguides that are compatible with conventional planar fabrication processes. For example, schemes to taper and route optical signals in

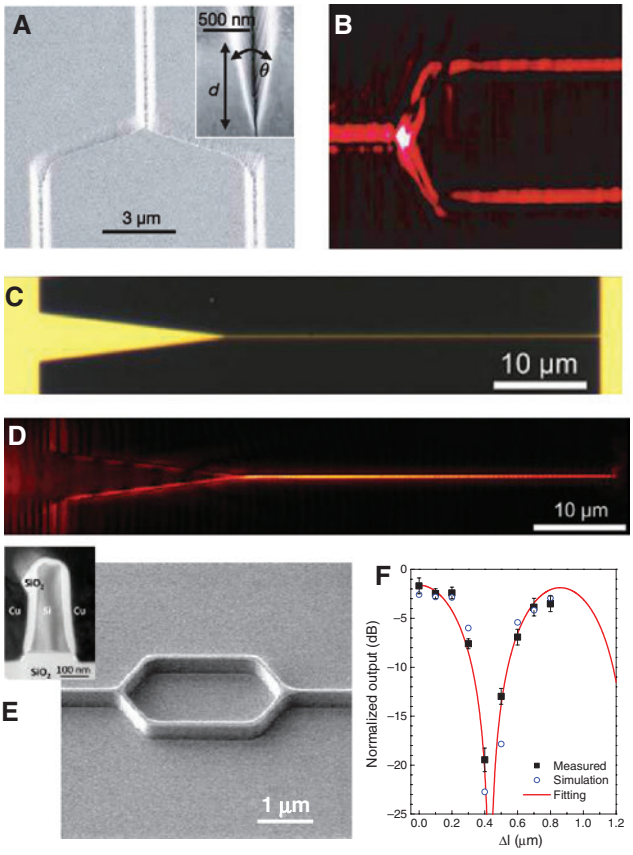

Figure 3: Passive integrated nanoplasmonic waveguide devices. (A) Scanning electron micrograph (SEM) of a channel plasmonic waveguide fabricated via 3D focused ion beam milling. (B) Scanning near-field optical microscope image of telecommunications signals propagating through a y-splitter. (A) and (B) are adapted from [45], with the permission of NPG. (C) Optical microscope image of an adiabatic taper used to confine signals to a Au nanowire. (D) Scanning near-field optical microscope image of fields being focused by the adiabatic taper and coupled to a 150 nm wide nanowire. (C) and (D) are adapted from [48], with the permission of APS. (E) SEM of a Mach-Zehnder interferometer fabricated with Cu-SiO_2-Si-SiO_2-Cu hybrid nanoplasmonic waveguides. The inset shows a cross-sectional slice of the waveguide geometry. (F) Signal transmission through Mach-Zehnder interferometer devices at $\lambda = 1550$ nm for varying length difference between the two interferometer arms. (E) and (F) are adapted from [50], with the permission of OSA.

metallic nanowires with dimensions as small as 40 nm have been developed, using a simple single-layer nanofabrication process. An exemplary device and scanning near-field microscopy field map are shown in Figure 3(C)–(D) [48, 49].

The dielectric-loaded SPP waveguide (DLW) consists of a metal film with rectangular dielectric waveguides patterned on top, which can be realized through simple nanofabrication processes. The geometry and mode profile for this waveguide are shown in Figure 4(A) and (B), respectively. The first in-depth characterization of this waveguide geometry revealed a propagation length of approximately 8 μm and routing in waveguides with cross-sectional dimensions as small as 300 nm was demonstrated [51]. Figure 4(C)–(D) depict a more advanced version of the DLW, known as the long-range DLW (LR-DLW). As the name implies, this design exhibits similar features as the LRSPP, namely a thin (~15 nm) metallic stripe sandwiched between two dielectric layers of similar refractive index. Although this design requires overlay alignment of an additional layer of lithography, its propagation losses are substantially lower than those of the DLW. Propagation lengths of 520 μm have been achieved at telecommunications wavelengths in Au stripes with $w = 500$ nm [52].

As discussed earlier, a dielectric material sandwiched between two metal layers is a commonly used geometry. The simplest realization of this geometry is a 2D slab-like structure, where subwavelength confinement exists in only one dimension. Signal transport over a 5 λ distance with $\lambda/5$ confinement has been demonstrated in Ag-Si_3N_4-Ag slab waveguides [53]. In subsequent work, a Au-Si-Au slot waveguide has been fabricated on the silicon-on-insulator (SOI) platform and integrated with Si photonic waveguides, thus providing subwavelength confinement in both lateral dimensions [54]. Measurement of $\lambda = 1.55$ μm laser light transmission through this waveguide revealed a propagation loss of 0.8 dB/μm [54]. More recently, broadband routing of telecommunications signals in Au-polymer-Au slot waveguides of various lengths revealed a propagation length of 5.56 μm (6 λ) [55, 56].

Two other common nanoplasmonic waveguide geometries are the metal-insulator (MI) configuration and the hybrid nanoplasmonic, or conductor-gap-Si, configuration. Schematic depictions of these geometries are shown in Figure 5(A)–(B), respectively; their respective mode profiles are shown in Figure 5(C)–(D). The asymmetry of the MI waveguide geometry gives rise to slightly poorer mode confinement than the slot waveguide geometry, but it still outperforms Si photonic waveguides in this regard.

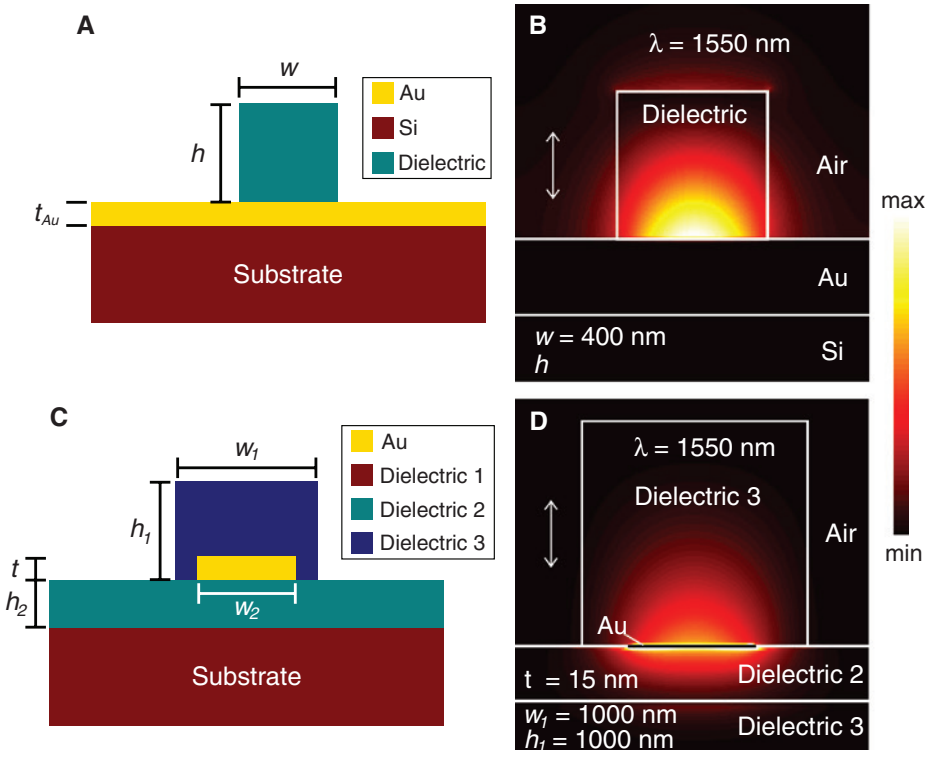

Figure 4: Dielectric-loaded SPP waveguides. (A) Schematic depiction of a DLW. (B) Mode profile of a DLW with $w = 400$ nm and $h = 400$ nm. (C) Schematic depiction of a LR-DLW. (D) Mode profile of LR-DLW with $w_1 = 1000$ nm, $h_1 = 1000$ nm, $t = 15$ nm, and $h_2 = 250$ nm.

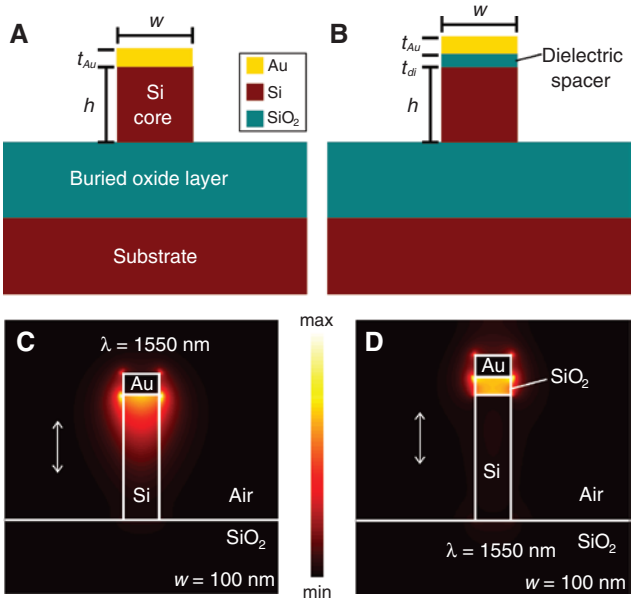

Figure 5: Metal-insulator and hybrid nanoplasmonic waveguides. (A) Schematic depiction of a metal-insulator (MI) nanoplasmonic waveguide with a Si core and Au cap. (B) Waveguide mode profile for the Au-Si waveguide with a width, $w = 100$ nm. (C) Schematic depiction of a metal-insulator-Si (MIS) nanoplasmonic waveguide with a Si core, SiO_2 spacer, and Au cap. (D) waveguide mode profile for the Au-SiO_2-Si waveguide with a width, $w = 100$ nm and a spacer thickness, $t_{di} = 50$ nm.

Metal-insulator waveguides consisting of Au and Si have been successfully integrated with SOI nanophotonic waveguides, and a propagation length of 2.0 μm has been measured for this platform [57].

The introduction of a thin low refractive index layer separating the metal features from the high-index waveguide core, as depicted in Figure 5(C), creates a hybrid plasmonic waveguide mode. Here, a highly-confined mode resembling a nanoplasmonic mode propagates in the low-index layer(s) and a photonic-like mode propagates in the high-index layer, as shown in Figure 5(D). This geometry not only enables confinement to sub-100 nm dimensions, but also increases the propagation length of the waveguide mode, because the photonic-like part of the waveguide mode experiences minimal interaction with the lossy metal layer. This waveguide class was first theoretically explored in the form of a gallium arsenide cylindrical nanowire separated from a Ag film by a thin SiO_2 layer, and was predicted to simultaneously enable strong confinement ($\lambda^2/400 - \lambda^2/40$) and long propagation distances (40–150 μm) [58]. Shortly after this, a hybrid nanoplasmonic waveguide consisting of a CdS nanowire, MgF_2 spacer layer, and Ag film is used to demonstrate the first nanoplasmonic laser [27]. This concept is subsequently implemented in a lithographically-defined Si-SiO_2-Au waveguide geometry and a propagation loss of 105 ± 5 cm^{-1} was measured [59]. More recently, a fully CMOS-compatible hybrid plasmonic device architecture, consisting of horizontally-arranged Cu-SiO_2-Si-SiO_2-Cu waveguides has been investigated in detail [50, 60–62]. Figure 3(E) displays this waveguide geometry, along with a Mach-Zehnder interferometer device fabricated on this platform. By varying the length difference between the two arms of the interferometer, the transmitted power was systematically altered via constructive or destructive interference, as shown in Figure 3(F). Finally, a comprehensive study of the propagation characteristics of metal-insulator-Si-insulator-metal waveguides, consisting of Au, Ag, or Cu metal layers and HfO_2 or SiO_2 insulator layers, revealed propagation lengths of up to 7.25 μm, where the modes are strongly confined to the 20 nm-thick insulator layers [63].

Ultimately, utilizing nanoplasmonic waveguides to bridge the dimensional gap between large photonic interconnects and electronic devices is desirable as it enables signal transduction between these two platforms. Using a Au-SiO_2-Au nanoplasmonic waveguide with 2D tapering, as shown in Figure 6(A), it has been demonstrated that signals at $\lambda = 800$ nm could be confined and routed in a waveguide having transverse dimensions of only 14×80 nm^2 [64]. More recently, a class of hybrid gap nanoplasmonic waveguides has been used to achieve routing in a volume of just 24×60 nm^2, where $\lambda = 1550$ nm signals could be transmitted through waveguides with lengths of $L = 5$ μm, as depicted in Figure 6(B) [65]. Using a similar tapering scheme, mid-infrared radiation at $\lambda = 9.3$ μm has been focused to a spot with a diameter of 60 nm, corresponding to $\lambda/150$ [66]. Other interesting developments have numerically demonstrated interfacing and impedance-matching between nanoplasmonic antennas and nanoplasmonic slot waveguides [67] and experimentally implemented nanoplasmonic slot waveguides in single-crystalline Au flakes [68].

3 Magnetoplasmonics

The incorporation of magnetic materials into optical devices provides a degree of control over modal properties, which is not attainable with other material systems. The interaction of light with a magnetized medium facilitates nonreciprocal phenomena, or optical effects that break the Lorentz reciprocity condition and the time-reversal symmetry, such as the Faraday effect or magneto-optical Kerr effect.

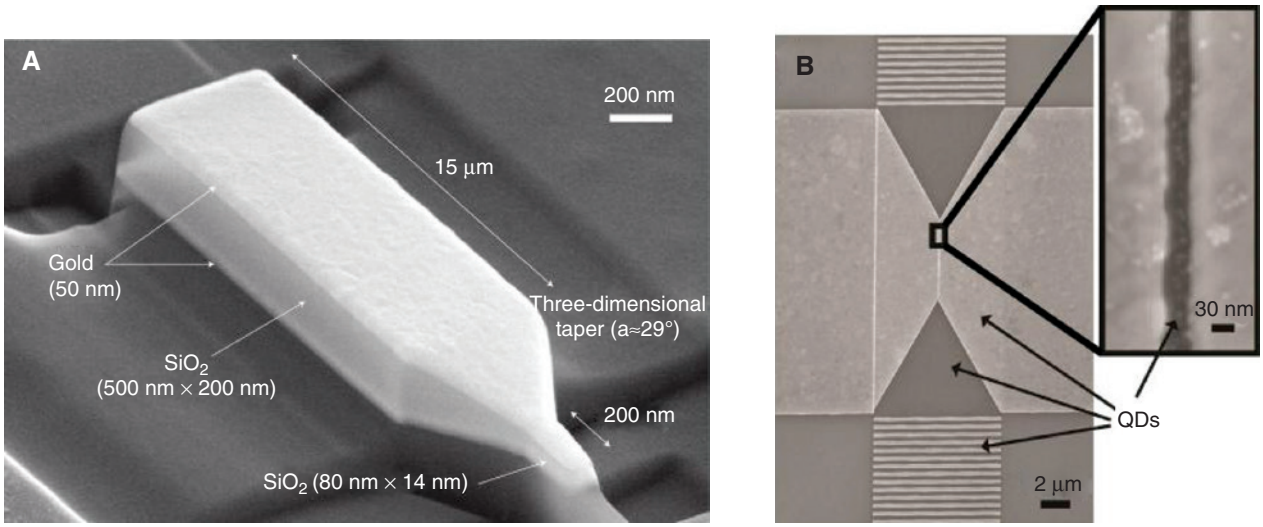

Figure 6: Nanoplasmonic signal routing at the sub-100 nm scale. (A) Au-SiO_2-Au nanoplasmonic waveguide tapered in the two lateral directions to 14×80 nm^2 dimensions. (A) is adapted from [64], with the permission of NPG. (B) Au-SiO_2-Au nanoplasmonic waveguide tapered to 24×60 nm^2 dimensions. (B) is adapted from [65], with the permission of ACS.

Magnetoplasmonic devices for use at optical frequencies can typically be separated into two categories depending on the material platform employed: those based on ferromagnetic metals, such as Fe, Ni, and Co, and those based on ferrimagnetic garnets, such as rare earth iron garnet. These material systems can produce appreciable magneto-optic effects under stimulus from weak magnetic fields, which can be practically generated for integrated applications. For completeness, we note here that doped semiconductors are utilized in the infrared and terahertz regimes; this technology has been extensively reviewed in the past [69, 70] and is not the focus of the present work.

Ferromagnetic metals exhibit significantly higher losses than conventional noble metals, and thus, they severely limit the propagation length when incorporated into plasmonic waveguides. For example, considering the dielectric function of the metal, $\varepsilon_m(\omega) = \varepsilon'_m(\omega) + i\varepsilon''_m(\omega)$, one can compare these materials using the quality factor of the SPP as a figure of merit, defined in Ref. [37] as $Q_{\mathrm{SPP}} = \varepsilon'_m(\omega)^2 / \varepsilon''_m(\omega)$. Materials with higher loss will have lower quality factors resulting from increased values of $\varepsilon''_m(\omega)$. Employing data from Refs. [71, 72], Q_{SPP} can be calculated to be 5149 for Ag and 1186 for Au, but only 53, 29, and 10 for Ni, Co, and Fe, respectively, at $\lambda = 1.55$ μm. Clearly, the figures of merit for ferromagnetic metals are several orders of magnitude smaller than those for Au and Ag, making them less appropriate for plasmonic waveguide devices due to the higher optical losses. Several methods have been investigated to mitigate this effect, such as the inclusion of a thin dielectric buffer inserted between the ferromagnetic metal and the plasmonic waveguide core [73], or embedding the thin ferromagnetic film within a noble metal layer. This multilayer architecture has led to a multitude of studies on the interaction between resonant plasmon excitation and magneto-optic phenomenon, many of which have been concisely summarized in Ref. [74].

Considering integrated magnetoplasmonic waveguide applications, ferrimagnetic garnets, such as YIG are an attractive material system. These materials are low-loss dielectrics (at telecommunication wavelengths) [75] that exhibit low saturation magnetization and can be incorporated with standard plasmonic metals. Additionally, YIG is characterized by strong magneto-optical properties, which can be enhanced by altering the chemical composition to include rare-earth ions [75]. Thus, during fabrication, the properties of the YIG can be tailored for the desired application.

The analysis of magnetoplasmonic waveguides has been carried out for decades. Specifically, a wide array of waveguide structures have been considered, including 2D planar MI interfaces [76], MIM slabs [77, 78], IMI slabs [79], and nanowires [80]. One key result of these analysis showed that the presence of a transverse static magnetic field over structures exhibiting some form of asymmetry (either in the geometry or magnetization profile) can cause the plasmon dispersion relation to split into two branches, corresponding to forward and backward propagating modes. Thus, the modal propagation constant (β) for a forward propagating mode is not equal to the

propagation constant for a backward propagating mode [i.e. $\beta_{fwd}(\omega) \neq \beta_{bwd}(\omega)$]. Such an effect breaks the Lorrentz reciprocity condition, and is nonreciprocal.

The nonreciprocity achieved by incorporating magnetic materials into plasmonic waveguides enables the construction of a fundamental optical component at the nanoscale – the optical isolator. The potential applicability of magnetoplasmons to optical isolators has been proposed in Refs. [79, 81]. Given that forward and backward propagating modes exhibit different propagation constants, a nonreciprocal phase shift (NRPS) between them, $\Delta\beta = \beta_{fwd} - \beta_{bwd}$, can be incorporated into Mach-Zehnder interferometers (MZIs) to create efficient isolators. However, as discussed in Ref. [81], the fundamental restriction is the propagation length of the surface mode, which is typically less than the length scale required to generate a significant $\pi/2$ NRPS because of the absorption losses in the metal. Thus, insertion losses on these devices were shown to be high. According to a previous study, long-range IMI structures could possibly mitigate this effect [79, 81].

This solution was realized recently with the presentation of a scheme based on long-range dielectric-loaded surface plasmon waveguides (LRDLSPWs) [82], as illustrated in Figure 7(A)–(B). By employing a Ce:YIG waveguide core, a thin Ag guiding strip, and dielectric buffer layers of Si_3N_4 and Al_2O_3, a LRDLSPW exhibiting a propagation length of over 3 mm was developed. Such a configuration is able to attain a $\pi/2$ NRPS within only 505.6 μm. Oppositely magnetized magnetoplasmonic waveguides were incorporated into the arms of a MZI, yielding an optical isolator with insertion losses of 2.5 dB and an extinction ratio of 22.8 dB.

Other configurations utilizing ferromagnetic metals, such as Fe as the plasmonic layer, have been proposed. One scheme utilized a $Fe/Al_2O_3/Si$ waveguide, where the thin Al_2O_3 film acts as a buffer between the Fe cap and Si core [85]. In this scheme, tailoring the thickness of the Al_2O_3

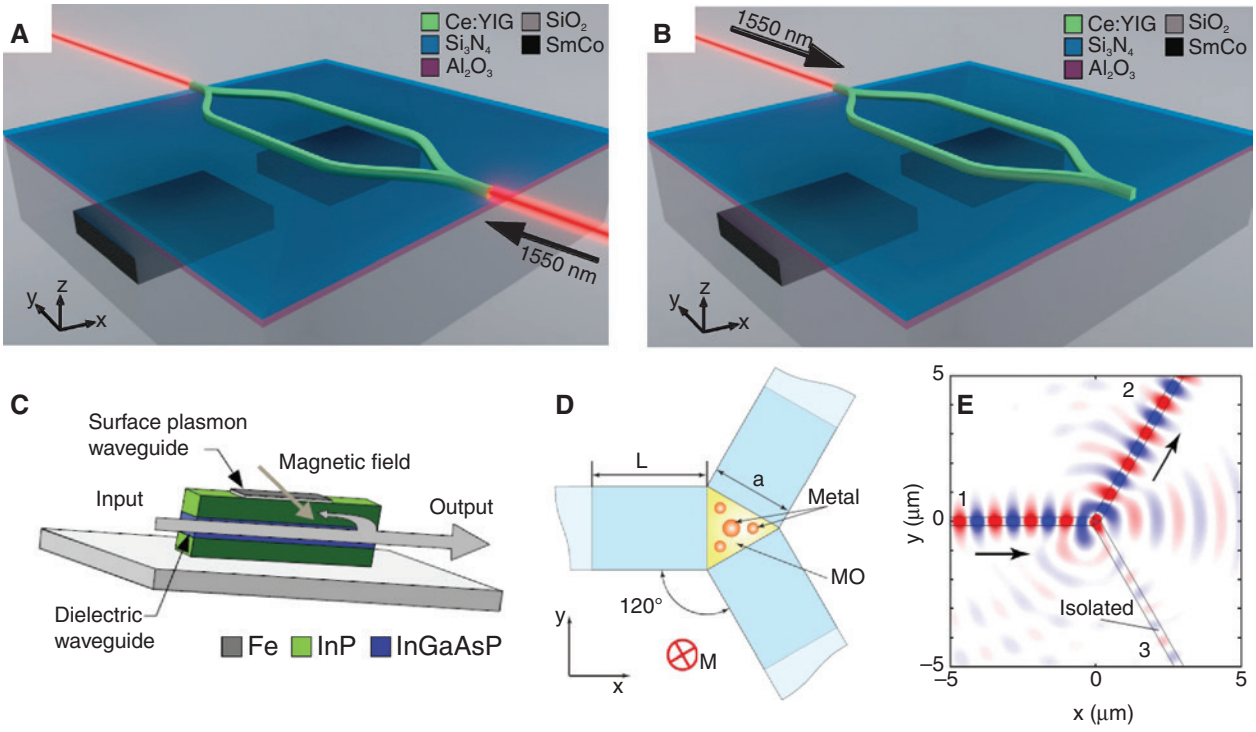

Figure 7: (A),(B) Integrated magnetoplasmonic isolator based on a long-range dielectric-loaded plasmonic waveguide geometry with an integrated samarium-cobalt (SmCo) magnet biasing scheme. (A) The device creates constructive interference for a forward propagating wave and (B) destructive interference for a backward propagating wave, yielding an isolation ratio of 22.8 dB. (A) and (B) are adapted from [82], with the permission of OSA. (C) Optical isolator based on nonreciprocal coupling between a guided photonic mode and a magnetoplasmonic mode. The structure is designed in such a way that the backwards propagating photonic mode couples to the Fe-InP magnetoplasmonic waveguide, and is strongly attenuated, while forward propagating photonic modes are uninhibited. Reproduced from [83], with the permission of AIP Publishing. (D) Magnetoplasmonic circulator consisting of Au nanorods embedded in a magneto-optic garnet cavity. (E) Operation of the magnetoplasmonic circulator. Under an applied magnetic field, the electromagnetic energy is efficiently directed from Port 1 to Port 2, while Port 3 remains isolated. (D) and (E) are reproduced from [84] in accordance with the Creative Commons Attribution 3.0 Unported (CC-BY) license.

film results in the mode being near cut-off, thus reducing losses and improving the potential isolation. Another scheme employs the nonreciprocal wavevector splitting to create a direction dependent coupling between a lossy magnetoplasmonic waveguide and a photonic waveguide [83]. In such a structure [shown in Figure 7(C)], the Fe-InP-InGaAsP-InP structure contains a Fe-InP magnetoplasmonic waveguide, and an InP-InGaAsP-InP photonic guide. The photonic mode and the backwards propagating magnetoplasmonic mode are phase matched, such that a backwards propagating photonic mode will couple into the plasmonic guide and be strongly attenuated by the Fe, whereas a forwards propagating mode is unaffected. As such, isolators with 3 dB insertion loss and 30 dB extinction ratios are proposed.

A natural extension to the development of two-port isolators is the development of three-port optical circulators. These components require nonreciprocal symmetry breaking to ensure that power injected at one port couples only into the next port around the device in a circular fashion. It has been theoretically shown that applying a magnetic field to a rare-earth iron garnet cavity, which contains a collection of Au nanorods causes the optical power to rotate around the embedded nanostructures [86]. The direction of the nonreciprocal power rotation could be reversed via magnetization reversal. Incorporating these magnetoplasmonic cavities at the junction of three waveguides, as depicted in Figure 7(D), it was shown that optical power could be directed between the output ports, producing an efficient optical circulator [84]. In this case [shown in Figure 7(E)], the magnetized device directed 63% of the input power (applied at Port 1) into Port 2, and only 3% into Port 3, whereas the unmagnetized device provided 33% of the input power to Ports 2 and 3.

Incorporating magnetic materials into nanoplasmonic structures provides a unique method of generating active, electrically controlled devices. Temnov et al. demonstrated this effect with a magnetoplasmonic slit-groove interferometer composed of an Au/Co/Au multilayer film [87, 88]. The plasmon excited by the groove interfered with radiation present in the nanoscale slit. With the application of a transverse, sinusoidally varying external magnetic field, the magnetization state of the buried Co film was modulated, and the nonreciprocal shift in the plasmon wavevector was modulated. Correspondingly, the wavevector shift was detected by the change in the interference pattern. While this interferometer was controlled via an external electromagnet, a recent work has shown that the insertion of a thin (2 nm) SiO_2 film between one of the Au films and the Co region electrically isolates the Au film, allowing it to function as an electrode [89]. Passing current through this electrode can generate the magnetic fields required for modulation of the Co magnetization, and hence the magneto-optic effects.

For the realization of integrated hybrid electronic-plasmonic circuitry, fabricating waveguides directly on top of the metal circuit traces is beneficial. As such, the electrical signals within the chip can serve a dual purpose: they can (1) simultaneously carry an electrical signal between components, and (2) generate the magnetic field required to encode data onto a plasmonic mode. Conventional dielectric-loaded plasmonic waveguides are ideal for such a task, as they are comprised of a ridge of dielectric set atop a metal slab. One such design employs a dielectric core of Bi:YIG deposited onto an Ag slab [90], illustrated in Figure 8(A). The phase shift in the optical mode could be switched via 100–500 ps current pulses passing through the underlying Ag. The electrically-induced magnetic field switched the magnetization and provided phase shifts of up to 0.34 rad from the initial state. This type of device has key applications for encoding data onto the phase of the mode via binary phase shift keying at speeds of up to 6 Gbit/s, as depicted in Figure 8(B).

This high-speed, dynamic phase modulation can be converted into intensity modulation with the use of an MZI [91] to facilitate the implementation of a new plasmonic logic element: the clock multiplier. Such a device is schematically illustrated in Figure 8(C). Here, LRDLSPWs were constructed from a Bi:YIG core, thin Ag guiding strip, and Si_3N_4 and Al_2O_3 buffer layers on a SiO_2 substrate. Parallel current pulses passing through two transmission lines adjacent to the interferometer arms produced transient magnetic fields capable of modulating the magnetization of the Bi:YIG core, and hence, the NRPS. Correspondingly, the interference condition at the output port was modulated, and hence, the signal was mapped into the output intensity. In this scheme, the device was driven in a resonant mode. A magnetic field pulse perturbed the statically biased magnetization vector, inducing a long-lasting, oscillatory precession as it relaxed back to its initial state, as shown in Figure 8(D). The frequency of such a precession was controlled by the magnitude of the longitudinal biasing field, and in this way, the device behaved as an optical analogue to an electrical clock multiplier. The input electrical pulse frequency was multiplied by factors of up to 2.1×10^3 upon mapping to the optical wave, and modulation depths over 16 dB were reported. Such a device has key applications in providing a mechanism of synchronizing both electrical and optical logic networks.

The aforementioned device geometry has proven to provide additional functionality when driven with

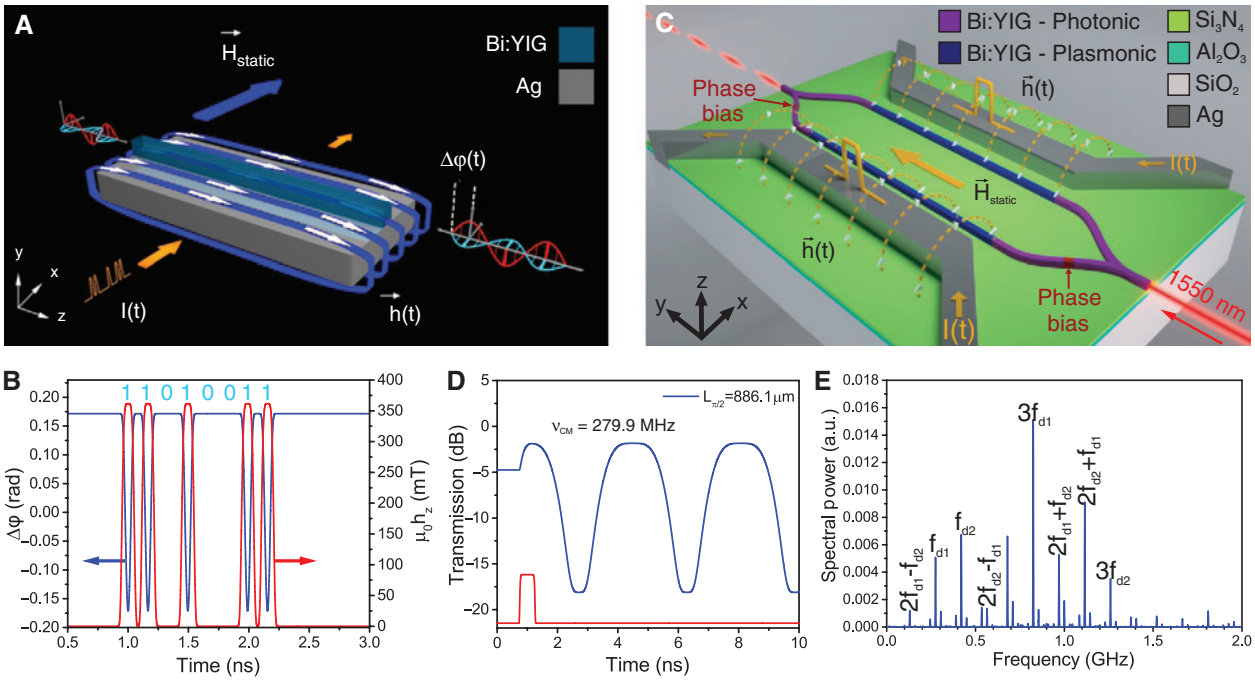

Figure 8: (A) Magnetoplasmonic waveguide phase shifter modulated by electric current passing through the underlying Ag slab. (B) Plot of the phase shift, $\Delta\varphi$, accumulated over the plasmonic mode propagation length of 49.06 μm. The blue lines depict $\Delta\varphi$, while the red lines indicate the 100 ps magnetic field pulses, encoding a binary signal 11010011. (A) and (B) are reproduced from [90], with the permission of OSA. (C) Magnetoplasmonic electrical-to-optical clock multiplier geometry that maps dynamic changes in the nonreciprocal phase shift into the intensity of the optical wave. (D) Clock multiplier transmission as a function of time upon excitation with a 500 ps magnetic field pulse of amplitude $\mu_0 h_z = 19$ mT in a static field of $\mu_0 H_y = 10$ mT. The output intensity oscillates with a frequency, $\nu_{CM} = 279.9$ MHz. The red curve represents the input magnetic field pulse, and is not represented to scale. (C) and (D) are reproduced from [91], with the permission of AIP Publishing. (E) Frequency spectrum of the modulated intensity output from the MZI when driven simultaneously by two sinusoidal signals with frequencies $f_{d1} = 700$ MHz and $f_{d2} = 1$ GHz. Both sinusoids have an amplitude of $\mu_0 h_z = 19$ mT, and are under a static bias of $\mu_0 H_y = 25$ mT. The spectrum contains third-order mixed frequencies of the two inputs. Reproduced from [92], with the permission of AIP Publishing.

sinusoidal RF signals instead of pulses [92]. Here, RF current signals passing through the transmission lines adjacent to the MZI continuously drive the magnetization of the Bi:YIG in a nonlinear manner. As such, the frequency spectrum of the modulated output intensity contains additional frequency components due to the nonlinear magnetization dynamics. Simulations have shown that the RF parameters could be optimized, such that the transmitted intensity signal contained harmonics of the input frequency, split the power between two different spectral components, down-converted the high-frequency input, or mixed multiple RF signals. One exemplary spectrum is depicted in Figure 8(E), depicting the mixed spectral components present when the device is driven at two frequencies, f_{d1} and f_{d2}, simultaneously.This unique modulator provides a tunable mechanism of attaining different modulation frequencies from a single device for integrated nanoplasmonic applications.

4 Nonlinear optics

4.1 Theoretical overview

For propagating nanoplasmonic waveguide modes with sufficiently strong electric fields, the electronic response to the time-varying electric field will become anharmonic. The anharmonicity of the electric polarization, P, can be expressed as a power series given by

$$P = \varepsilon_0[\chi^{(1)}E + \chi^{(2)}E^2 + \chi^{(3)}E^3 + \ldots], \tag{5}$$

where $\varepsilon_0 = 8.85 \times 10^{-12}$ F/m is the permittivity of free space, E is the electric field strength, and $\chi^{(n)}$ is the n^{th} order electric susceptibility. In the electric field regime, in which the nonlinear response is a simple perturbation to the linear one, $P^{(2)} = \varepsilon_0\chi^{(2)}E^2$ and $P^{(3)} = \varepsilon_0\chi^{(3)}E^3$ constitute the primary nonlinear optical signals. Notably, $\chi^{(2)}$ is zero for any centrosymmetric material, and as a result, $\chi^{(3)}$ is the dominant

nonlinear interaction in many common dielectrics and metals. An exception to this occurs at material interfaces, which inherently lack inversion symmetry [93], in strained systems, wherein a deviation from perfect crystal lattice periodicity breaks the inversion symmetry [94], or when asymmetry is induced with a sufficiently strong static electric field [95].

The second order nonlinear polarization, $P^{(2)}$, results in nonlinear wave mixing interactions including second-harmonic generation (SHG), sum-frequency generation (SFG), difference-frequency generation (DFG), and optical rectification. Meanwhile, the third order nonlinear polarization, $P^{(3)}$, expresses third-order nonlinear wave mixing and nonlinear loss. Third-harmonic generation (THG) occurs when a photon of frequency 3ω is generated from three incident photons of frequency ω, i.e. nonlinear wave mixing at the third-harmonic frequency. The optical Kerr effect represents nonlinear wave mixing at the fundamental frequency and brings about a nonlinear refractive index given by

$$n = n_0 + n_2 I, \tag{6}$$

where n is the effective refractive index of the medium, n_0 is the linear refractive index, n_2 is the optical Kerr coefficient, and I is the optical intensity.

Two-photon absorption (TPA) is a nonlinear loss process, whereby two incident photons have sufficient energy to promote an electron from the valence band to the conduction band, which may also require a phonon for momentum conservation if the material has an indirect bandgap. As shown below, the total loss of the material system depends linearly on the optical intensity

$$\alpha = \alpha_0 + \beta_{\mathrm{TPA}} I, \tag{7}$$

where α is the total loss and α_0 is the linear loss. The nonlinear loss can be effectively used for signal modulation or saturation of propagating signals. In the presence of a significant free-carrier density, additional incident photons can be absorbed through free-carrier absorption (FCA).

4.2 Nonlinear optics in nanoplasmonic waveguides

In general, nonlinear interactions in nanoplasmonic waveguides occur simultaneously in the plasmonic metal and in the adjacent dielectrics. The relative contribution of each constituent material to the nonlinear signal strength depends on the magnitude of the relevant nonlinear coefficients in the material and on the fraction of the nanoplasmonic waveguide mode propagating through that material. Nonlinear interactions in Si photonic waveguides have undergone extensive experimental investigations, including TPA, THG, and self- and cross-phase modulation [96–119]. Despite extensive numerical simulations indicating promising prospects, nonlinear interactions in nanoplasmonic waveguides have remained elusive in the experimental realm, presumably because of additional practical challenges involved in the fabrication and direct nonlinear characterization of the nanoscale waveguides.

Although SHG and THG in nanoplasmonic waveguides have been investigated numerically by several groups [120–122], to date, there has only been a single experimental report of optical harmonic generation. As depicted in Figs. 9(A)–(B), Si-Au MI nanoplasmonic waveguides were fabricated in a unique scheme that allowed for direct end-fire excitation of the waveguide input facets and direct outcoupling of the nonlinear signals from the waveguide output facets [123]. Using this configuration, $\lambda = 1550$ nm laser pulses were upconverted to $\lambda = 517$ nm third-harmonic signals with efficiencies up to $\eta_{\mathrm{THG}} = 2.3 \times 10^{-5}$ [124], as shown in Figs. 9(C)–(D). Despite the absorption of the 3ω signal in the Si and a large phase-mismatch between the fundamental and 3ω signal, this marks the highest third-harmonic conversion efficiency in any Si photonic or nanoplasmonic waveguide device.

For the appropriate combination of material and wavelength, achieving nonlinear signal modulation in the plasmonic metal features is possible. Free-space pumping of an aluminum plasmonic waveguide with $\lambda = 780$ nm pulses, depicted schematically in Figure 10(A), was used to alter the optical properties of the aluminum film on an ultrafast timescale, modulating the amplitude of signals propagating through the nanoplasmonic waveguide [125]. Modulation on two timescales was demonstrated through pump-probe measurements: $\tau_1 = 200$ fs and $\tau_2 = 60$ ps. The fast response (τ_1), displayed in Figure 10(B), was sensitive to the polarization orientation of the pump pulses relative to that of the propagating plasmonic modes and was only observed when the two polarizations were parallel to one another. This dynamic arises from non-parabolicity of the electron bands and the resulting anharmonic electron oscillations of the propagating plasmon. The slow response (τ_2), plotted in Figure 10(C), was independent of the pump polarization orientation, and was identified as the cause of interband electron transitions and the subsequent electron thermalization dynamics.

All-optical signal modulation can be realized by modifying the optical properties of a dielectric or semiconductor adjacent to a metal film. A tapered plasmonic waveguide has been used to enhance visible upconversion and observe interference patterns from plasmonic focusing

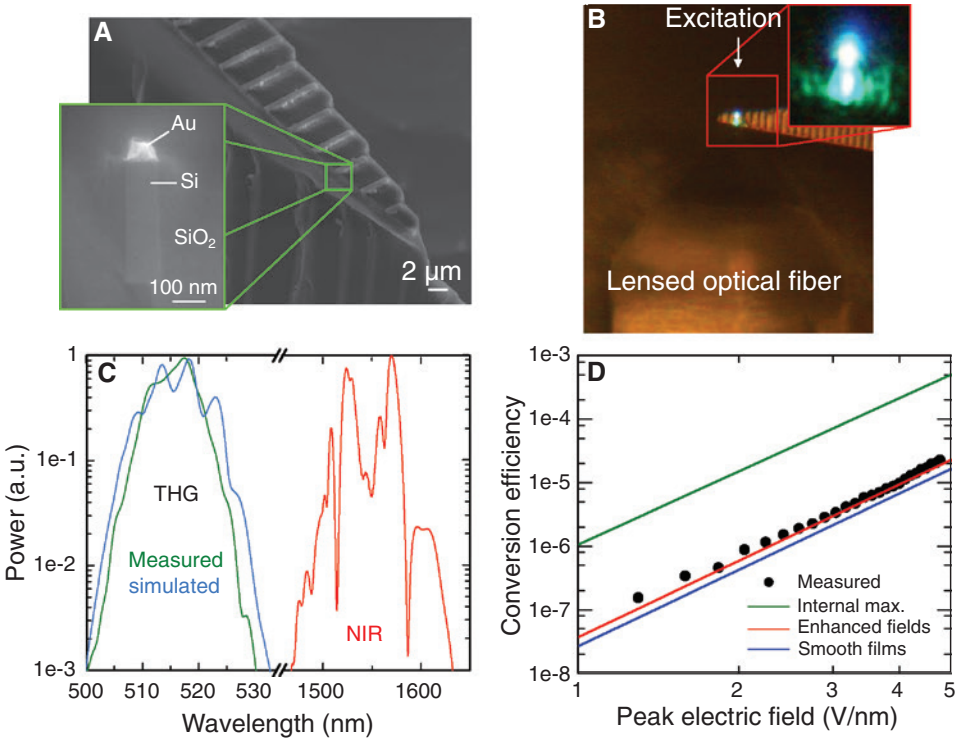

Figure 9: Third-harmonic generation in a Si-loaded nanoplasmonic waveguide. (A) Scanning electron micrograph of Si-loaded nanoplasmonic waveguides integrated onto a deeply-etched characterization beam. (B) Top-view optical microscope image of visible light emission from the Si-loaded nanoplasmonic waveguides when excited by $\lambda = 1550$ nm pulses. (C) Spectra of the fundamental and third-harmonic pulses. (D) Measured and simulated THG conversion efficiencies as a function of fundamental electric field strength. (A)–(D) are adapted from [124], with the permission of APS.

near the interface between silver and erbium-doped sapphire films [19, 126]. Figure 11(A) portrays an experimental arrangement whereby telecommunications signals are coupled to a grating at a Au-Si interface, and free-space pumping at $\lambda = 775$ nm is used to excite charge carriers in the Si material, modulating the telecommunications signal transmission [127]. In principle, free-carriers can have two effects: (1) they contribute additional nonlinear loss to the signal transmission via free-carrier absorption; and (2) they alter the refractive index of the Si material via plasma dispersion and as a result, they shift the resonant coupling conditions of the telecommunications to the grating. The broadband coupling efficiency of the grating as a function of time-delay is plotted in Figure 11(B). As can be seen in the figure, the resonant coupling conditions of the grating are shifted by more than their spectral width, confirming this as the primary contribution to the modulation. As the free-carriers recombined at surface states of the Si material, the resonant coupling condition was restored to its initial state and pump-probe measurements were used to demonstrate a device recovery time of $\tau = 103$ ps, as shown in Figure 11(C). Numerical investigations employing ultrafast free-carrier excitation in Si have demonstrated the feasibility of achieving modulation in straight nanoplasmonic waveguides via plasma-induced loss [128] and in nanoring resonators through free-carrier dispersion [129, 130]. In addition, electrical control of the free-carrier density in CMOS-compatible hybrid nanoplasmonic waveguides has been used to achieve electroabsorption modulation [131] and phase modulation [132], although the modulation bandwidth is inherently limited by that of the electrical circuitry.

Recently, a new technique to sensitively measure nonlinear spectral broadening in nanophotonic and nanoplasmonic waveguides has been demonstrated [133]. Briefly, the scheme is based on detecting newly generated spectral components of the pulse with a high signal-to-noise ratio. Before being coupled into the waveguide, each pulse was passed through a spectral filter, such that a sharp spectral edge was introduced to the pulse. After spectral broadening in the waveguide, the pulse was spectrally filtered again, enabling only the newly generated spectral components to be measured. Using this scheme, the authors report a nonlinear signal from hybrid nanoplasmonic waveguides that is slightly weaker, but on the same order of magnitude, as a nonlinear signal measured

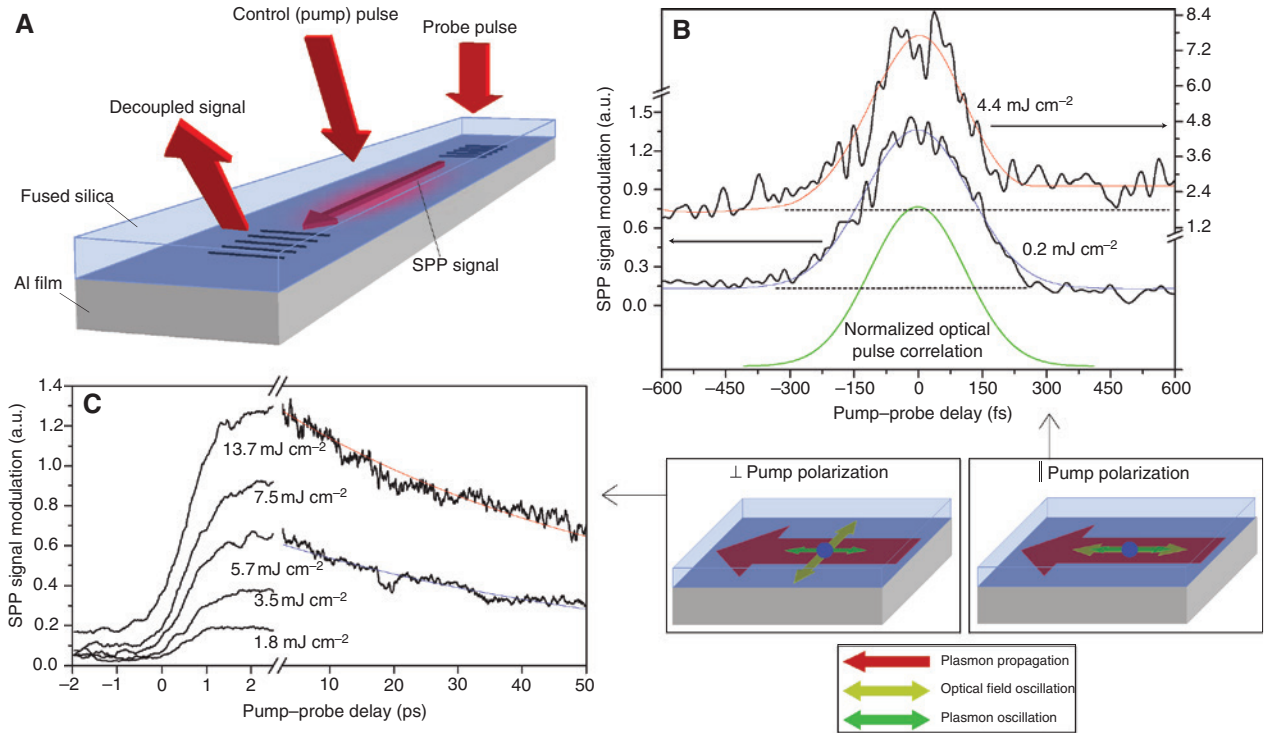

Figure 10: Ultrafast all-optical modulation in an aluminium plasmonic waveguide. (A) Schematic representation of the waveguide geometry and the pump-probe scheme. (B) Fast response measured when the pump polarization was parallel to that of the plasmon oscillation, exhibiting $\tau_1 = 200$ fs. (C) Slow response, $\tau_2 = 60$ ps observed when the pump polarization was perpendicular to the plasmon oscillation. (A)–(C) are adapted from [125], with the permission of NPG.

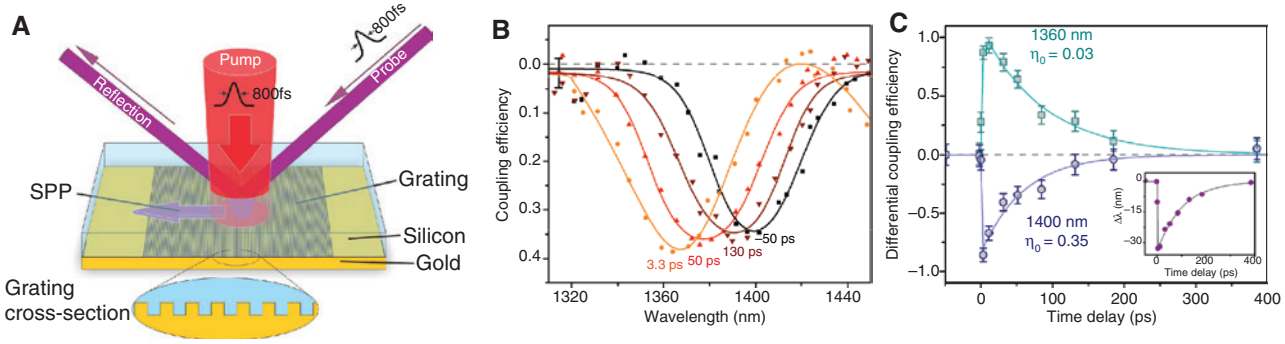

Figure 11: Ultrafast all-optical control of the resonant coupling conditions of a silicon-based plasmonic grating. (A) Schematic representation of the grating geometry and the pump-probe configuration. (B) Broadband coupling efficiency of the grating for relative pump-probe delays of $\Delta t = -50$ ps, 3.3 ps, 50 ps, and 130 ps. (C) Ultrafast grating coupling dynamics at $\lambda = 1360$ nm and $\lambda = 1400$ nm, revealing a device recovery timescale of $\tau = 103$ ps. (A)–(C) are adapted from [127], with the permission of OSA.

from a Si photonic waveguide. These results are summarized in Figure 12. Although the linear propagation losses of the nanoplasmonic mode weaken the nonlinear signal, this work further demonstrates the potential for generating nonlinear signals in a deeply subwavelength volume.

The inclusion of metallic features in the geometry of nanoplasmonic waveguides enables natural electrodes to perform electro-optic phase modulation. Electro-optic modulation in resonant devices, including nanoslits [134], Mach-Zehnder interferometers [135], ring resonators, [136], donut resonators [137], and stub filters [138], has been investigated in several numerical studies. Recently, electro-optic modulation was experimentally demonstrated in a 29 μm long polymer-loaded nanoplasmonic waveguide at a bandwidth of 40 Gbit s^{-1} [9], as shown in Figure 13(A)–(B). Subsequently, a 10 μm long Mach-Zehnder consisting

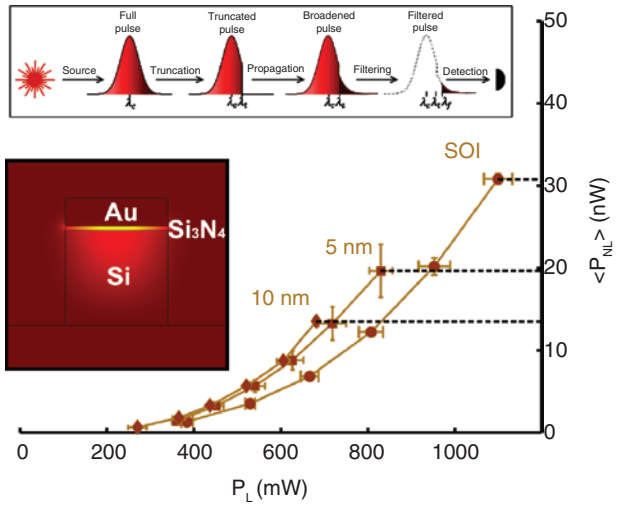

Figure 12: Measurement of nonlinear spectral broadening in hybrid nanoplasmonic waveguides for varying input power and Si_3N_4 gap thicknesses, and a baseline comparison with a SOI waveguide. The top inset depicts the measurement approach, consisting of spectral pre-filtering, nonlinear spectral broadening in the waveguide structure, and spectral post-filtering for sensitive detection of nonlinear signal generation. The left inset depicts the hybrid nanoplasmonic waveguide mode profile. Images adapted from [133], with the permission of OSA.

of polymer-loaded nanoplasmonic waveguides was used to demonstrate electro-optic modulation at a bandwidth of 72 Gbit s^{-1} and an estimated power consumption of 25 fJ bit^{-1} [139], as shown in Figure 13(C)–(D).

5 Strong-field devices

For increasing electric field strengths, new regimes are encountered and corresponding new effects can be observed. By exploiting extreme ultrafast nonlinear effects in waveguide devices, the strong field regime can be accessed within an integrated, chipscale, nanoplasmonic platform. Notably, atomic electric field strengths are on the order of

$$E_{at} = \frac{e/4\pi\varepsilon_0}{a_0^2} = 5.14\times10^{11}\,\mathrm{V/m}, \tag{8}$$

where $e = 1.602\times10^{-19}$ C is the amplitude of the charge of an electron, and $a_0 = 5.2918\times10^{-11}$ m is the Bohr radius of a hydrogen atom. For electric fields that are not insignificant relative to E_{at}, the series expansion of Eq. 5 no longer converges, marking the onset of the non-perturbative, strong-field, or extreme nonlinear regimes. For such fields, the response of valence band electrons is no longer determined by the low-energy bandstructure. Large conduction band electron populations can be excited, and these electrons can be accelerated high into the energy bands and to the edge of the Brillouin zone, where they may be reflected or tunnel into another band. Alternatively, electrons can be ejected into vacuum where they interact with the intense laser fields in a ballistic manner and can be accelerated to high energies.

5.1 Ponderomotive electron acceleration

When a free electron interacts with an intense electromagnetic field possessing a high spatial gradient, the former can undergo ponderomotive electron acceleration [140]. This interaction is characterized by a cycle-by-cycle acceleration, resulting from a net ponderomotive force due to the asymmetry of the field. Briefly, free electrons are initially accelerated, on the first half-cycle of the electric field, from a region of high electric field to an area of lower electric field, i.e. along the gradient of the electric field. On the next subsequent half-cycle, the electron is then decelerated, but by an amount less than on the first half-cycle. Over many cycles, this phenomenon results in a net ponderomotive force being set up in the direction of the gradient of the electric field, with the electron being accelerated to a higher velocity and hence, a higher kinetic energy. Without a high spatial gradient, this force will cancel out over multiple cycles, thus producing no net acceleration or deceleration.

In order to achieve the necessary asymmetric electric field, ponderomotive electron acceleration has been studied using a variety of platforms including: strong-field laser electron acceleration in vacuum [141–143], surface plasmon electron acceleration on metallic films and nanostructures [144–146], and within nanoplasmonic semiconductor devices [147, 148]. For the purpose of this review, the focus is on nanoscale devices as the other methods are inherently macroscale and require high-intensity amplified laser pulses ($I \geq 10^{12}$ W/cm^2). For the case of compact, integrated, strong-field devices, the semiconductor platform of choice is Si. Si was chosen for its many advantages, including CMOS compatibility, ease of fabrication, and its high $\chi^{(3)}$ non-linearity, which allow for efficient free electron generation.

The ponderomotive potential energy is a measure of the kinetic energy acquired by an electron during one oscillation of the laser field and is expressed as

$$U_P = \frac{e^2}{4m_e^*\omega^2}E_0^2, \tag{9}$$

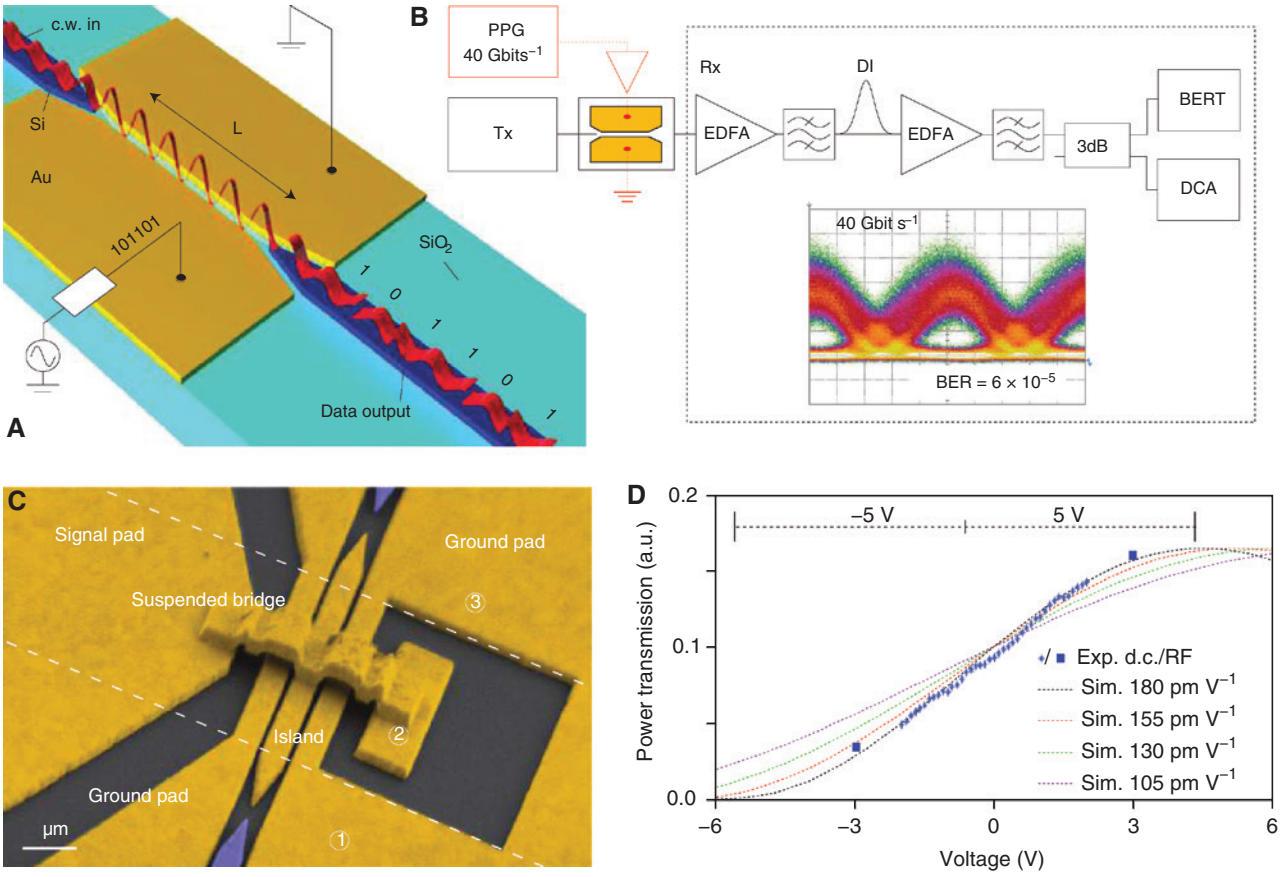

Figure 13: Electro-optic modulation in nanoplasmonic waveguides. (A) Schematic depiction of a polymer-loaded nanoplasmonic slot waveguide where an electric voltage signal is applied between the two metal sidewalls of the waveguide. (B) Experimental configuration used to measure the inset eye diagram at 40 Gbit s^{-1}. (A)–(B) are adapted from [9], with the permission of NPG. (C) False-colour SEM of an electro-optic phase shifter used to achieve signal modulation in a Mach-Zehnder interferometer fabricated from polymer-loaded nanoplasmonic waveguides. (D) Optical power transmission for varying voltage. (C)–(D) are adapted from [139], with the permission of NPG.

where ω is the angular frequency of the driving laser field, and E_0 is the electric field strength of the driving laser field. For example, Si has an effective electron mass, $m_e^* = 2.37 \times 10^{-31}$ kg. If we consider a laser wavelength of $\lambda = 1550$ nm, corresponding to $\omega = 1.22 \times 10^{15}$ rad/s, and an electric field strength of $E_0 = 5$ V/nm, a ponderomotive potential energy of $U_P = 2.75$ eV is calculated. Notably, the ponderomotive potential scales quadratically with both E_0 and λ of the driving laser field, making intense pulses at longer wavelengths desirable for accessing strong-field effects.

5.2 Visible light emission from a nanoplasmonic waveguide

A combination of strong light confinement and electric field enhancement offered by nanoplasmonic waveguides enables the investigation of novel strong field phenomena in a technologically relevant device platform. Considering again an MI waveguide geometry consisting of a Si waveguide core and an Au nanoplasmonic cap, the strong field regime can be easily reached using nJ laser pulses available from turnkey fiber lasers [148]. Moreover, the distribution of electric fields in the waveguide mode profile is highly asymmetric, making it an ideal structure for ponderomotive electron acceleration. As mentioned in the previous section, when moderate electric field strengths on the order of $E_0 \sim 1$ V/nm interact with conduction band electrons in Si, they reach energies on the order of several eV during one laser field oscillation. Notably, the threshold for impact ionization in Si is $E_t = 2.3$ eV, thereby suggesting interesting dynamics in the electron population, namely avalanche multiplication. Naturally, electron motion in the Si lattice is not ballistic; rather, collisions occur with a mean free path of $l_c = 28$ nm. Regardless, electron trajectories can be calculated using the time-domain electric fields propagating

through the nanoplasmonic waveguide geometry and the classical equation of motion

$$v(t) = v_i(t_0) + \int_{t_0}^{t} \frac{eE(t)}{m_e^*} \mathrm{d}t, \tag{10}$$

where $v(t)$ is the instantaneous velocity of the electron, $v_i(t_0)$ is the initial velocity imparted to the electron by any excess excitation energy, and $E(t)$ is the time-varying electric field propagating through the waveguide. Using these simulations, electron trajectories at random injection positions and times are easily simulated, and sample trajectories are shown in Figure 14(A). In the case of a Si bandgap energy of $E_g = 1.1$ eV and a laser wavelength of $\lambda = 1550$ nm, free-carriers will be excited via TPA and the corresponding rate equation can be written as

$$\frac{\mathrm{d}N(\vec{r}, t)}{\mathrm{d}t} = \frac{\beta_{\mathrm{TPA}}}{2h\nu} I^2(\vec{r}, t), \tag{11}$$

where N is the free-carrier density, $h = 6.626 \times 10^{-34}$ m^{2}kg/s is the Planck constant, and ν is the laser frequency. Using this rate equation and the electron trajectories, an electron energy spectrum representing a weighted distribution of the average kinetic energy of each calculated electron trajectory can be calculated. The results for three different electric field strengths are shown in Figure 14(B).

Notably, electrons are easily accelerated to energies exceeding the threshold for impact ionization before undergoing their first collision. This finding demonstrates that the conditions required for a non-destructive electron avalanche are met. This interaction is summarized in Figure 14(C) and the dynamics are briefly summarized as follows: (i) electron-hole pairs are excited via TPA in the Si core of the nanoplasmonic waveguide; (ii) they are born into the intense fields of the nanoplasmonic waveguide mode and they are accelerated in a cycle-by-cycle fashion and many of them reach energies exceeding the threshold for impact ionization; (iii) the electron-hole population grows exponentially as the more mobile electrons undergo multiple impact ionization events. One other noteworthy observation from the simulated electron trajectories is that a majority of the electrons – particularly the most energetic ones – have a primary velocity component in the direction normal to the Au-Si interface, suggesting interesting time dynamics in the electron density distribution both during the acceleration phase and after the pulse has passed.

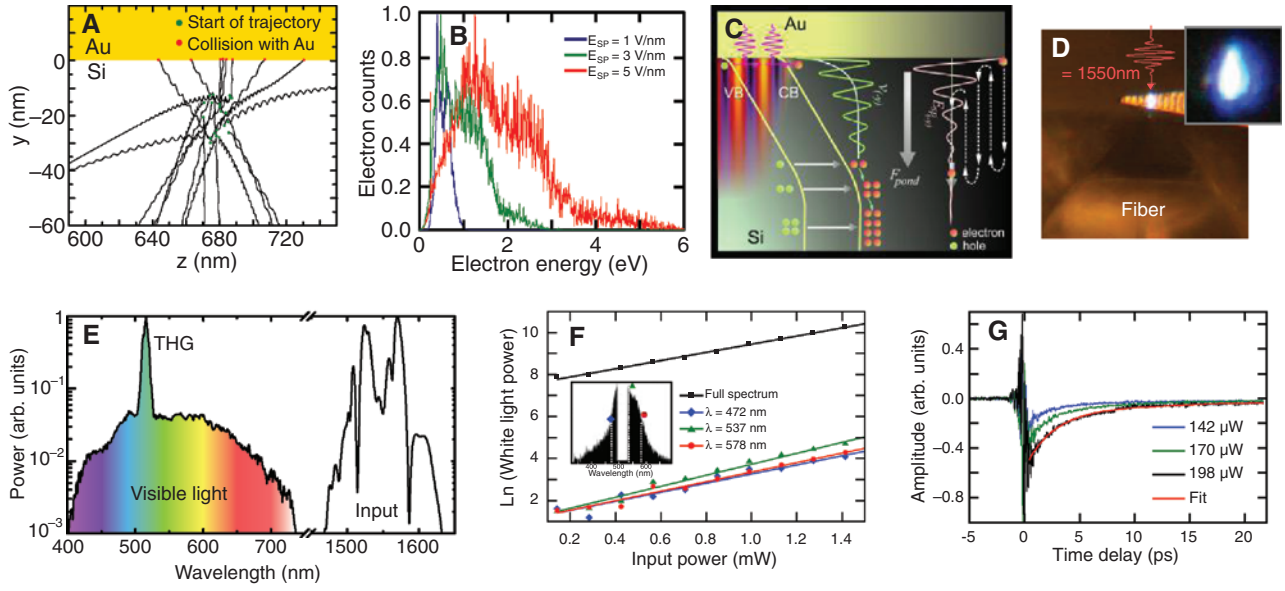

Figure 14: Ponderomotive electron acceleration in a Si-loaded nanoplasmonic waveguide. (A) Sample trajectories of electrons excited via TPA in the nanoplasmonic waveguide as they interact with the remainder of the $\lambda = 1550$ nm laser pulse. (B) Electron energy spectrum representing the average energies achieved by electrons during their first 28 nm of motion. (C) Schematic illustration of the sequence of physical processes leading to avalanche multiplication of the free electron population. Electrons are excited from the valence band (VB) to the conduction band (CB) via TPA. In this way, they are now free to interact with the intense nanoplasmonic fields, E_{SP}, which exert a ponderomotive force, F_{pond}. The electrons are easily accelerated to a velocity, v, which corresponds to a kinetic energy exceeding the threshold for impact ionization. Through multiple impact ionization events, the free-carrier population multiplies exponentially. (D) Top-view optical microscope image of bluish-white light emission from the Si-loaded nanoplasmonic waveguide. (E) Spectra of the fundamental laser pulse, THG, and broadband white light emission. (F) Power scaling of the white light emission shown on a logarithmic y-axis. (G) Pump-probe measurement of free-carrier sweeping dynamics. (A)–(G) are adapted from [148], with the permission of APS.

This interaction can be probed in two different ways: (1) measurement of visible light emission from the Au-Si nanoplasmonic waveguides, and (2) pump-probe measurements designed to measure the temporal dynamics of the electron density distribution. Both measurements were performed using laser pulses of $\tau_p = 84$ fs duration at $\lambda = 1550$ nm. Intense white light emission was collected from the output facet of the Si-loaded nanoplasmonic waveguide, as shown in Figure 14(D). The measured spectrum is shown in Figure 14(E). The power scaling of the white light, which exhibits a distinctly exponential trend, is shown on a logarithmic *y*-axis in Figure 14(F). This white light is a biproduct of collisions that occur as the electron-hole population multiplies through the avalanche process, and provides a qualitative measure of the electron-hole population as a function of input power. This light emission demonstrates a broadband, highly-localized light source on a nanoplasmonic chip.

The temporal dynamics of the electron density distribution are measured by coupling two pulses into the waveguide in a pump-probe configuration and a sample trace is shown in Figure 14(G). In this scheme, the pump pulse excites electron-hole pairs and imparts them with a velocity normal to the Au-Si interface, while the other pulse probes the instantaneous electron density in the immediate region of the nanoplasmonic mode profile. Therefore, as the probe pulse is delayed such that it arrives after the pump pulse, its transmission will recover as electrons are swept out of the mode region. A recovery on two timescales is observed: $\tau_1 = 1.98$ ps and $\tau_2 = 17.9$ ps. The τ_1 timescale matches very well to what would be expected from electrons being swept out of the waveguide mode region and traveling at the saturation velocity of Si, $v_s = 1.3 \times 10^5$ m/s, which would yield a displacement of $\Delta = 257$ nm away from the Au-Si interface. The avalanche multiplication and ultrafast recovery are ideal for sensitive and high bandwidth detection of nanoplasmonic pulses and their transduction to short electrical pulses.

5.3 Ultrafast nanoplasmonic triode

In order to fully integrate plasmonic circuits with current day electronics, various electronic functions must be realized in a nanoplasmonic platform. This platform can operate with the speed of photonic circuits, while possessing the footprint of modern nanoelectronics. Furthermore, such a platform bridges the gap between photonics and electronics. Adaptation of the above mentioned nanoplasmonic waveguide structure used for visible light emission has been proposed by Greig and Elezzabi in order to design an ultrafast nanoplasmonic triode device [147]. This triode is the nanoscale optical analogue to the first vacuum tube devices that sparked the modern technological era. The device operates via the acceleration and subsequent filtering of two-photon absorption generated electrons in the Si core.

Briefly, the nanoplasmonic waveguide structures consists of upper and lower Cu claddings on a Si core, with a tungsten (W) grid placed in the core, Figure 15(A). Electrons that are generated in the Si core by two-photon absorption of the nanoplasmonic electric field at the upper Cu cladding are ponderomotively accelerated towards the bottom Cu electrode. When driven with an 84 fs laser pulse, the electrons arrive at the electrode within 150 fs, demonstrating ultrafast switching. During their transit, the electrons must pass through the W grid. As the electrons are able to gain a range of kinetic energies as they reach the grid,

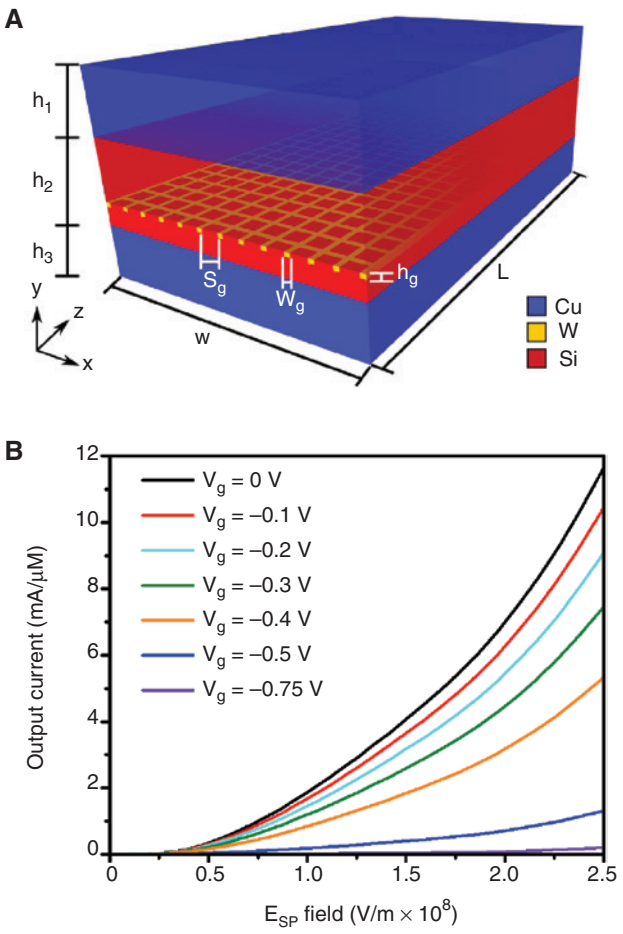

Figure 15: 3D schematic of silicon nanoplasmonic triode with the following dimensions: $h_1 = 60$ nm, $h_2 = 30$ nm, $h_3 = 100$ nm, $w_g = 4$ nm, $h_g = 3$ nm, $s_g = 4$ nm, w, and $L = 350$ nm. (B) Characteristic output current curves of the nanoplasmonic triode. Reproduced from [147] with the permission of AIP Publishing.

a kinetic energy filter can be used to limit the number of electrons passing through the grid, and hence the total current collected at the bottom electrode. This kinetic energy filter is realized by applying a bias voltage, V_g, between the grid and the upper Cu electrode. Similarly, the total number of generated electrons can be controlled by varying the strength of the nanoplasmonic electric field, E_{SP}. By varying both V_g and E_{SP}, triode-like behavior can be achieved, Figure 15(B). Remarkably, an output current of 11.7 mA/μm can be achieved at $E_{SP}=2.5\times10^8$ V/m, with the output dropping to 0.2 mA/μm with an applied $V_g=-0.75$ V.

5.4 Ultrafast nanoplasmonic carrier-envelope-phase detector

When working with ultrashort laser pulses that consist only of a few cycles of the oscillating electric field, the carrier-envelope-phase (CEP) becomes important. Future nanoplasmonic devices that exploit the CEP of plasmons may be able to introduce a new information processing paradigm. By combining the confinement of the electric field with coherent CEP detection, the nanoplasmonic platform will open the way for new methods of quantum communication and encryption. Currently, to measure single shot CEP, a laser pulse ionizes a gas jet and the CEP is extracted by measuring the subsequent current difference between left and right electron detectors [149, 150]. Another highly sensitive and simple technique to measure the absolute CEP of pulses spanning the telecommunications to terahertz spectral regions is electro-optic sampling, whereby a high-frequency probe pulse is used to measure the temporal structure of a low-frequency waveform [151]. As each of these methods require quite large, complicated, experimental setups, developing an ultrafast, nanoplasmonic method of detecting single shot CEP is important.

A solid-state equivalent to the ionized gas jet method, which utilizes a semiconductor for the electron generation medium is currently being explored. Figure 16(A) depicts a cartoon illustration of the device consisting of a 50 nm-thick Au antenna embedded in the top layer of a Si substrate, with a 20 nm gap between the antenna point and the transmission line. Electrons were generated in the Si within the gap by 800 nm laser pulses. These electrons were then subsequently ponderomotively accelerated towards either the left or the right electrode, based on the asymmetry of the electric field at the tip of the nanoantenna. As this interaction was highly dependent on the CEP of the driving laser pulse, a difference in current between the two electrodes was obtained for varying

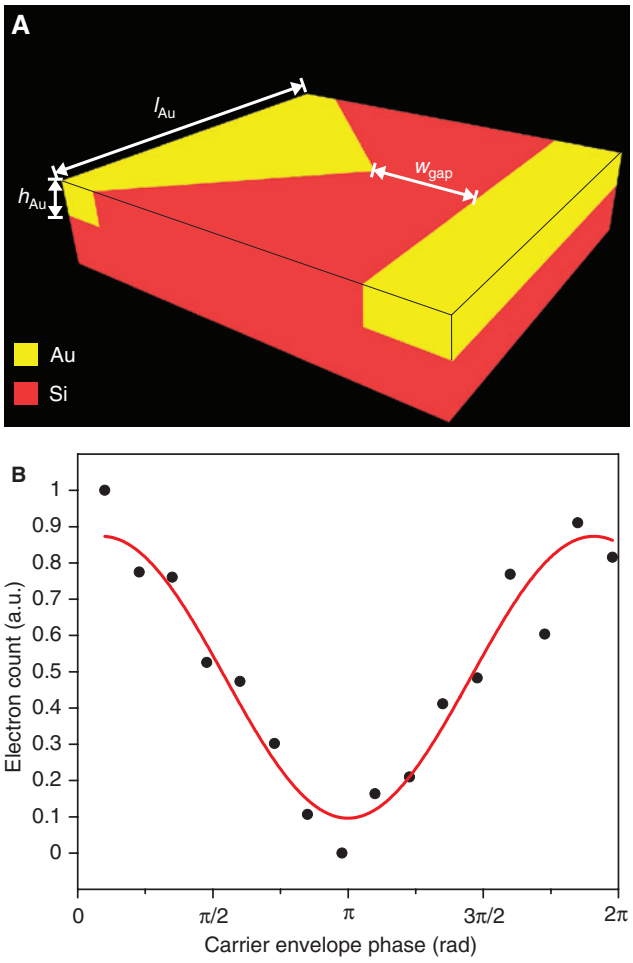

Figure 16: (A) 3D schematic of silicon CEP detector with dimensions $w_{gap}=20$ nm, $h_{Au}=50$ nm, $l_{Au}=200$ nm. (B) Output current response as a function of CEP. The red line represents a sinusoidal fit.

values of CEP. Preliminary simulation results, depicted in Figure 16(B), indicate that the detected current follows the expected sinusoidal behavior. This device represents a compact method for direct measurement of the CEP of a laser pulse from low intensity oscillators.

5.5 Perspectives on strong-field devices

Nanoscale devices harnessing strong-field laser-electron interactions in semiconductors show promise for the next generation of optical computing devices. Specifically, semiconductor ponderomotive electron acceleration allows for increased switching speeds by moving free carriers via light instead of a conventional, externally applied, electrical bias. This, in turn, opens up a new platform that revisits the operating principles of the original vacuum tubes, except operating at significantly increased

speeds (terahertz), owing to the electrons being driven by surface plasmon fields.

6 Conclusions and outlook

Since early investigations of long-range surface plasmon polariton waveguides, plasmonic waveguides have experienced successful advances in confining and routing electromagnetic energy to ever-smaller dimensions, approaching those of modern electronic circuitry. Simultaneously, plasmonic waveguides have enjoyed diversification in functionality, and devices based on nonlinear optical frequency conversion, nonlinear optical modulation, magneto-optical modulation, and strong-field interactions have undergone rapid development. While some devices have successfully been implemented using common nanofabrication materials and techniques, others have only been understood numerically and are being intensively implemented in physical form. Despite the ever increasing research interest, a major issue facing the widespread adoption of nanoplasmonic devices for next-generation optical computing is the high costs associated with their fabrication. Generally, fabrication of nanoplasmonic devices requires the use of either electron-beam lithography or focused ion beam milling to define the waveguide structures. These methods are slow and operate on the chip-scale, which is in stark contrast to the fast, wafer-scale processing of optical lithography currently employed in the nanoelectronics industry. Additionally, to achieve full compatibility with nanoelectronics, the metals used in nanoplasmonic devices need to change from the noble metals to copper or aluminum. As copper and aluminum are more lossy, this characteristic must be accounted for in the design of the devices. Furthermore, nanoplasmonic devices cannot currently achieve the integration densities of nanoelectronics due to the 100 nm width of the waveguides and the potential for crosstalk when the waveguides are brought too close together. However, as the operation of various constituent devices is understood and optimized to a technologically relevant level, it will become necessary to implement their monolithic integration with one another, with the low-loss Si photonic platform, and with modern electronic circuitry.

References

[1] Miller DAB. Device requirements for optical interconnects to silicon chips. Proc IEEE 2009;97:1166–85.
[2] Maier SA. Plasmonics: fundamentals and applications. Springer US, 2007.
[3] Ditlbacher H, Aussenegg FR, Krenn JR, Lamprecht B, Jakopic G, Leising G. Organic diodes as monolithically integrated surface plasmon polariton detectors. Appl Phys Lett 2006;89:161101.
[4] Akimov AV, Mukherjee A, Yu CL, et al. Generation of single optical plasmons in metallic nanowires coupled to quantum dots. Nature 2007;460:402–6.
[5] Neutens P, Van Dorpe P, De Vlaminck I, Lagae L, Borghs G. Electrical detection of confined gap plasmons in metal-insulator-metal waveguides. Nature Photon 2009;3:283–6.
[6] Dionne JA, Diest K, Sweatlock LA, Atwater HA. PlasMOStor: a metal-oxide-Si field effect plasmonic modulator. Nano Lett 2009;9:897–902.
[7] Dionne JA, Sweatlock LA, Sheldon MT, Alivisatos P, Atwater HA. Silicon-based plasmonics for on-chip photonics. IEEE J Sel Top Quantum Electron 2010;16:295–306.
[8] Walters RJ, van Loon RVA, Brunets I, Schmitz J, Polman A. A silicon-based electrical source of surface plasmon polaritons. Nature Mater 2010;9:21–5.
[9] Melikyan A, Alloatti L, Muslija A, et al. High-speed plasmonic phase modulators. Nature Photon 2014;8:229–33.
[10] Stockman MI. Nanoplasmonics: past, present, and glimpse into future. Opt Express 2011;19:22029–106.
[11] Willets KA, Van Duyne RP. Localized surface plasmon resonance spectroscopy and sensing. Annu Rev Phys Chem 2007;58:267–97.
[12] Novotny L, van Hulst N. Antennas for light. Nature Photon 2011;5:83–90.
[13] Crozier KB, Sundaramurthy A, Kino GS, Quate CF. Optical antennas: resonators for local field enhancement. J Appl Phys 2003;94:4632.
[14] Li K, Stockman MI, Bergman DJ. Self-similar chain of metal nanospheres as an efficient nanolens. Phys Rev Lett 2003;91:227402.
[15] Stockman MI. Nanofocusing of optical energy in tapered plasmonic wasveguides. Phys Rev Lett 2004;93:137404.
[16] Mühlschlegel P, Eisler HJ, Martin OJF, Hecht B, Pohl DW. Resonant optical antennas. Science 2005;10:1607–9.
[17] Bharadwaj P, Anger P, Novotny L. Nanoplasmonic enhancement of single-molecule fluorescence. Nanotechnology 2006;18:044017.
[18] Hanke T, Krauss G, Träutlein D, Wild B, Bratschitch R, Leitenstorfer A. Efficient nonlinear light emission of single gold optical antennas driven by few-cycle near-infrared pulses. Phys Rev Lett 2009;103:257404.
[19] Verhagen E, Polman A, Kuipers L. Nanofocusing in laterally tapered plasmonic waveguides. Phys Rev Lett 2009;102:203904.
[20] Sederberg S, Elezzabi AY. Sierpinski fractal plasmonic antenna: a fractal abstraction of the plasmonic bowtie antenna. Opt Express 2011;19:10456–61.
[21] Sederberg S, Elezzabi AY. Nanoscale plasmonic contour bowtie antenna operating in the mid-infrared. Opt Express 2011;19:15532–7.
[22] Sederberg S, Elezzabi AY. The influence of Hausdorff dimension on plasmonic antennas with Pascal's triangle geometry. Appl Phys Lett 2011;98:261105.
[23] Ciraci C, Hill RT, Mock JJ, et al. Probing the ultimate limits of plasmonic enhancement. Science 2012;337:1072–4.

[24] Berman DJ, Stockman MI. Surface plasmon amplication by stimulated emission of radiation: quantum generation of coherent surface plasmons in nanosystems. Phys Rev Lett 2003;90:027402.
[25] Ambati M, Nam SH, Ulin-Avila E, Genov DA, Bartal G, Zhang X. Observation of stimulated emission of surface plasmon polaritons. Nano Lett 2008;8:3998–4001.
[26] Hill MT, Marell M, Leong ESP, et al. Lasing in metal-insulator-metal sub-wavelength plasmonic waveguides. Opt Express 2009;17:11107–12.
[27] Oulton RF, Sorger VJ, Zentgraf T, et al. Plasmon lasers at deep subwavelength scale. Nature 2009;461:629–32.
[28] De Leon I, Berini P. Amplification of long-range surface plasmons by a dipolar gain medium. Nature 2010;4:382–7.
[29] Berini P, De Leon I. Surface plasmon-polariton amplifiers and lasers. Nature Photon 2012;6:16–24.
[30] Kéna-Cohen S, Stravinou PN, Bradley DDC, Maier SA. Confined surface plasmon-polariton amplifiers. Nano Lett 2013;13:1323–9.
[31] Sidiropoulos TPH, Röder R, Geburt S, et al. Ultrafast plasmonic nanowire lasers near the surface plasmon frequency. Nature Phys 2014;10:870–6.
[32] Rotenberg N, Kuipers L. Mapping nanoscale light fields. Nature Photon 2014;8:919–26.
[33] Cortes CL, Newman W, Molesky S, Jacob Z. Quantum nanophotonics using hyperbolic metamaterials. J Opt 2012;14:063001.
[34] Engheta N, Ziolkowksi RW. Metamaterials: physics and engineering explorations. New York: Wiley, 2006.
[35] Han Z, Bozhevolnyi SI. Radiation guiding with surface plasmon polaritons. Rep Prog Phys 2013;76:016402.
[36] Krasavin AV, Zayats AV. Active nanophotonic circuitry based on dielectric-loaded plasmonic waveguides. Adv Opt Mater 2015;3:1662–90.
[37] West PR, Ishii S, Naik GV, Emani NK, Shalaev VM, Boltasseva A. Searching for better plasmonic materials. Laser Photonics Rev 2010;4:795–808.
[38] Kinsey N, Ferrera M, Shalaev VM, Boltasseva A. Examining nanophotonics for integrated hybrid systems: a review of plasmonic interconnects and modulators using traditional and alternative materials. J Opt Soc Am B 2015;32:121–42.
[39] Babicheva VE, Boltasseva A, Lavrinenko AV. Transparent conducting oxides for electro-optical plasmonic modulators. Nanophotonics 2015;4:165–85.
[40] Berini P. Figures of merit for surface plasmon waveguides. Opt Express 2006;14:13030–42.
[41] Buckley R, Berini P. Figures of merit for 2D surface plasmon waveguides and application to metal stripes. Opt Express 2007;15:12174–82.
[42] Charbonneau R, Berini P, Berolo E, Lisicka-Shrzek E. Experimental observation of plasmon-polariton waves supported by a thin metal film of finite width. Opt Lett 2000;25:844–6.
[43] Berini P, Charbonneau R, Lahoud N, Mattiussi G. Characterization of long-range surface-plasmon-polariton waveguides. J Appl Phys 2005;98:043109.
[44] Pile DFP, Ogawa T, Gramotnev DK, et al. Theoretical and experimental investigation of strongly localized plasmons on triangular metal wedges for subwavelength waveguiding. Appl Phys Lett 2005;87:061106.
[45] Bozhevolnyi SI, Volkov VS, Devaux E, Lalulet JY, Ebbesen TW. Channel plasmon subwavelength waveguide components including interferometers and ring resonators. Nature 2006;440:508–11.
[46] Volkov VS, Bozhevolnyi SI, Devaux E, Lalulet JY, Ebbesen TW. Wavelength selective nanophotonic components utilizing channel plasmon polaritons. Nano Lett 2007;7:880–4.
[47] Boltasseva A, Volkov VS, Nielsen RB, Moreno E, Rodrigo SG, Bozhevolnyi SI. Triangular metal wedges for subwavelength plasmon-polariton guiding at telecom wavelengths. Opt Express 2008;16:5252–60.
[48] Verhagen E, Spasenovic M, Polman A, Kuipers L. Nanowire plasmon excitation by adiabatic mode transformation. Phys Rev Lett 2009;102:203904.
[49] Dikken DJ, Spasenovic M, Verhagen E, van Oosten D, Kuipers L. Characterization of bending losses for curved plasmonic nanowire waveguides. Opt Express 2010;18:16112–9.
[50] Zhu S, Lo GQ, Kwong DL. Components for silicon plasmonic nanocircuits on horizontal Ci-SiO_2-Si-SiO_2-Cu nanoplasmonic waveguides. Opt Express 2012;20:5867–81.
[51] Steinberger B, Hohenau A, Ditlbacher H, Aussenegg FR, Leitner A, Krenn JR. Dielectric stripes on gold as surface plasmon waveguides. Appl Phys Lett 2006;88:094104.
[52] Volkov VS, Han Z, Nielsen MG, et al. Long-range dielectric-loaded surface plasmon polariton waveguides operating at telecommunications wavelengths. Opt Lett 2011;36:4278–80.
[53] Dionne JA, Lezec HJ, Atwater HA. Highly confined photon transport in subwavelength metallic slot waveguides. Nano Lett 2006;6:1928–32.
[54] Chen L, Shakya J, Lipson M. Subwavelength confinement in an integrated metal slot waveguide on silicon. Opt Lett 2006;31:2133–5.
[55] Han Z, Elezzabi AY, Van V. Experimental realization of subwavelength plasmonic slot waveguides on a silicon platform. Opt Lett 2010;35:502–4.
[56] Han Z, Elezzabi AY, Van V. Wideband Y-splitter and aperture-assisted coupler based on sub-diffraction confined plasmonic slot waveguides. Appl Phys Lett 2010;96:131106.
[57] Sederberg S, Van V, Elezzabi AY. Monolithic integration of plasmonic waveguides into a complimentary metal-oxide-semiconductor- and photonic-compatible platform. Appl Phys Lett 2010;96:121101.
[58] Oulton RF, Sorger VJ, Genov DA, Pile DFP, Zhang X. A hybrid plasmonic waveguide for subwavelength confinement and long-range propagation. Nature Photon 2008;2:496–500.
[59] Goykhman I, Desiatov B, Levy U. Experimental demonstration of locally oxidized hybrid silicon-plasmonic waveguide. Appl Phys Lett 2010;97:141106.
[60] Zhu S, Lo GQ, Kwong DL. Experimental demonstration of vertical Cu-SiO_2-Si hybrid plasmonic waveguide components on an SOI platform. IEEE Technol Lett 2012;24:1224–6.
[61] Zhu S, Lo GQ, Kwong DL. Performance of ultracompact copper-capped silicon hybrid plasmonic waveguide-ring resonators at telecom wavelengths. Opt Express 2012;20:15232–46.
[62] Kwon MS, Shin JS. Investigation of 90° submicrometer radius bends of metal-insulator-silicon-insulator-metal waveguides. Opt Lett 2014;39:715–8.
[63] Nielsen MP, Elezzabi AY. Plasmonic materials for metal-insulator-semiconductor-insulator-metal nanoplasmonic waveguides on silicon-on-insulator platform. Opt Mater 2013;36:294–8.

[64] Choo H, Kim MK, Staffaroni M, et al. Nanofocusing in a metal-insulator-metal gap plasmon waveguide with a three-dimensional linear taper. Nature Photon 2012;6:838–44.
[65] Nielsen MP, Lafone L, Rakovitch A, et al. Adiabatic nanofocusing in hybrid gap plasmon waveguides on the silicon-on-insulator platform. Nano Lett 2016;16:1410–4.
[66] Schnell M, Alonso-Gonzalez P, Arzubiaga L, et al. Nanofocusing of mid-infrared energy with tapered transmission lines. Nature Photon 2011;5:283–7.
[67] Huang JS, Feichtner T, Biagioni P, Hecht B. Impedance matching and emission properties of nanoantennas in an optical nanocircuit. Nano Lett 2009;9:1897–902.
[68] Huang JS, Callegari, Geisler P, et al. Atomically flat single-crystalline gold nanostructures for plasmonic nanocircuitry. Nature Commun 2010;1:150.
[69] Kushwaha MS. Plasmons and magnetoplasmons in semiconductor heterostructures. Surf Sci Rep 2001;41:1–416.
[70] Hu B, Zhang Y, Wang QJ. Surface magneto plasmons and their applications in the infrared frequencies. Nanophotonics 2015;4:383–96.
[71] Johnson PB, Christy RW. Optical constants of noble metals. Phys Rev B 1972;6:4370–9.
[72] Johnson PB, Christy RW. Optical constants of transition metals: Ti, V, Cr, Mn, Fe, Co, Ni, and Pd. Phys Rev B 1974;9:5056–70.
[73] Zayets V, Saito H, Ando K, Yuasa S. Long-distance propagation of a surface plasmon on the surface of a ferromagnetic metal. Opt Express 2015;23:12834–39.
[74] Armelles G, Cebollada A, García-Martín A, González MU. Magnetoplasmonics: combining magnetic and plasmonic functionalities. Adv Optical Mater 2013;1:10–35.
[75] Zvezdin AK, Kotov VA. Modern magnetooptics and magnetooptical materials. Bristol: IOP Publishing, 1997.
[76] Chiu KW, Quinn JJ. Magneto-plasma surface waves in solids. Il Nuovo Cimento B. 1972;10:1–20.
[77] Nikolova D, Fisher AJ. Switching and propagation of magnetoplasmon polaritons in magnetic slot waveguides and cavities. Phys Rev B 2013;88:125136.
[78] Ferreiro-Vila E, García-Martín JM, Cebollada A, Armelles G, González MU. Magnetic modulation of surface plasmon modes in magnetoplasmonic metal-insulator-metal cavities. Opt Express 2013;21:4917–30.
[79] Sepúlveda B, Lechuga LM, Armelles G. Magnetooptic effects in surface-plasmon-polaritons slab waveguides. J Lightwave Technol 2006;24:945–55.
[80] Davoyan A, Engheta N. Electrically controlled one-way photon flow in plasmonic nanostructures. Nat Commun 2014;5:5250.
[81] Khurgin JB. Optical isolating action in surface plasmon polaritons. Appl Phys Lett 2006;89:251115.
[82] Firby CJ, Elezzabi AY. Magnetoplasmonic isolators utilizing the nonreciprocal phase shift. Opt Lett 2016;41:563–6.
[83] Montoya J, Parameswaran K, Hensley J, Allen M, Ram R. Surface plasmon isolator based on nonreciprocal coupling. J Appl Phys 2009;106:023108.
[84] Davoyan A, Engheta N. Nanoscale plasmonic circulator. New J Phys 2013;15:083054.
[85] Zayets V, Saito H, Ando K, Yuasa S. Optical isolator utilizing surface plasmons. Materials 2012;5:857–71.
[86] Davoyan A, Engheta N. Nonreciprocal rotating power flow within plasmonic nanostructures. Phys Rev Lett 2013;111:047401.
[87] Temnov VV, Armelles G, Woggon U, et al. Active magneto-plasmonics in hybrid metal-ferromagnet structures. Nat Photonics 2010;4:107–11.
[88] Temnov VV. Ultrafast acousto-magneto-plasmonics. Nat Photonics 2012;6:728–36.
[89] Gong Y, Li K, Carver S, et al. Current control of light by nonreciprocal magnetoplasmonics. Appl Phys Lett 2015;106:191104.
[90] Firby CJ, Elezzabi AY. High-speed nonreciprocal magnetoplasmonic waveguide phase shifter. Optica 2015;2:598–606.
[91] Firby CJ, Elezzabi AY. A magnetoplasmonic electrical-to-optical clock multiplier. Appl Phys Lett 2016;108:051111.
[92] Firby CJ, Elezzabi AY. Magnetoplasmonic RF mixing and nonlinear frequency generation. Appl Phys Lett 2016;109:011101.
[93] Wang FX, Rodriguez FJ, Albers WM, Ahorinta R, Sipe JE, Kauranen M. Surface and bulk contributions to the second-order nonlinear optical response of a gold film. Phys Rev B 2009;80;233402.
[94] Cazzanelli M, Bianco F, Borga E, et al. Second-harmonic generation in silicon waveguides strained by silicon nitride. Nature Mater 2012;11:148–54.
[95] Cai W, Vasudev AP, Brongersma ML. Electrically controlled nonlinear generation of light with plasmonics. Science 2011;333:1720–3.
[96] Dekker R, Usechak N, Först M, Driessen A. Ultrafast nonlinear all-optical processes in silicon-on-insulator waveguides. J Phys D: Appl Phys 2007;40:R249–71.
[97] Tsang HK, Wong CS, Liang TK, et al. Optical dispersion, two-photon absorption and self-phase modulation in silicon waveguides at 1.5 μm wavelength. Appl Phys Lett 2002;80:416–8.
[98] Rieger GW, Virk KS, Young JF. Nonlinear propagation of ultrafast 1.5 μm pulses in high-index-contrast silicon-on-insulator waveguides. Appl Phys Lett 2004;84:900–3.
[99] Cowan AR, Rieger GW, Young JF. Nonlinear transmission of 1.5 μm pulses through single-mode silicon-on-insulator waveguide structures. Appl Phys Lett 2004;12:1611–21.
[100] Boyraz O, Koonath P, Raghunathan V, Jalali B. All optical switching and continuum generation in silicon waveguides. Opt Express 2004;12:4094–102.
[101] Boyraz O, Indukuri T, Jalali B. Self-phase-modulation induced spectral broadening in silicon waveguides. Opt Express 2004;12:829–34.
[102] Liang T, Nunes LR, Sakamoto T, et al. Ultrafast all-optical switching by cross-absorption modulation in silicon wire waveguides. Opt Express 2005;13:7298–303.
[103] Espinola RL, Dadap JI, Osgood RM, McNab SJ, Vlasov YA. C-band wavelength conversion in silicon photonic wire waveguides. Opt Express 2005;13:4341–9.
[104] Fukuda H, Yamada K, Shoji T, et al. Four-wave mixing in silicon wire waveguides. Opt Express 2005;13:4629–37.
[105] Moss DJ, Fu L, Littler I, Eggleton BJ. Ultrafast all-optical modulation via two-photon absorption in silicon-on-insulator waveguides. Electron Lett 2005;41:320–1.
[106] Dulkeith E, Vlasov YA, Chen C, Panoiu NC, Osgood RM. Self-phase-modulation in submicron sillicon-on-insulator photonic wires. Opt Express 2006;14:5524–34.
[107] Hsieh IW, Chen X, Dadap JI, et al. Ultrafast-pulse self-phase modulation and third-order dispersion in Si photonic wire-waveguides. Opt Express 2011;19:20172–81.

[108] Dekker R, Driessen A, Wahlbrink T, Moormann C, Niehusmann J, Först M. Ultrafast Kerr-induced all-optical wavelength conversion in silicon waveguides using 1.55 μm femtosecond pulses. Opt Express 2006;14:8336–46.
[109] Lin Q, Zhang J, Fauchet PM, Agrawal GP. Ultra-broadband parametric generation and wavelength conversion in silicon waveguides. Opt Express 2006;14:4786–99.
[110] Foster MA, Turner AC, Sharping JE, Schmidt BS, Lipson M, Gaeta AL. Broad-band optical parametric gain on a silicon photonic chip. Nature 2006;441:960–3.
[111] Foster MA, Turner AC, Salem R, Lipson M, Gaeta AL. Broad-band continuous wave parametric wavelength conversion in silicon nanowaveguides. Opt Express 2007;15:12949–58.
[112] Hsieh IW, Chen X, Liu X, et al. Supercontinuum generation in silicon photonic wires. Opt Express 2007;15:15242–9.
[113] Salem R, Foster MA, Turner AC, Geraghty DF, Lipson M, Gaeta AL. Signal regeneration using low-power four-wave mixing on a silicon chip. Nature Photon 2008;2:35–8.
[114] Zlatanovic S, Park JS, Moro S, et al. Mid-infrared wavelength conversion in silicon waveguides using ultracompact telecom-band-derived pump source. Nature Photon 2010;4:561–4.
[115] Kuyken B, Liu X, Osgood RM, Baets R, Roelkens G, Green WMJ. Mid-infared to telecom-band supercontinuum generation in highly nonlinear silicon-on-insulator waveguides. Opt Express 2011;19:20172–81.
[116] Lau RKW, Menard M, Okawachi Y, et al. Continuous-wave mid-infrared frequency conversion in silicon nanowaveguides. Opt Lett 2011;36:1263–5.
[117] Motamedi AR, Nejadmalayeri AH, Khilo A, Kärtner F, Ippen EP. Ultrafast nonlinear optical studies of silicon nano-waveguides. Opt Express 2012;20:4085–101.
[118] Sederberg S, Elezzabi AY. Nonlinear response of an ultra-compact waveguide Fabry-Pérot resonator. Appl Phys Lett 2013;102:011133.
[119] Sederberg S, Elezzabi AY. Nonmonotonic wavelength-dependent power scaling in silicon-on-insulator waveguides via nonlinear optical effect conglomeration. ACS Photonics 2014;1:576–81.
[120] Lu FF, Li T, Hu XP, Cheng QQ, Zhu SN, Zhu YY. Efficient second-harmonic generation in nonlinear plasmonic waveguide. Opt Lett 2011;36:3371–3.
[121] Zhang J, Cassan E, Gao D, Zhang X. Highly efficient phase-matched second harmonic generation using and asymmetric plasmonic slot waveguide configuration in hybrid polymer-silicon photonics. Opt Express 2013;21:14876–87.
[122] Wu T, Sun Y, Shao X, Shum PP, Huang T. Efficient phase-matched third harmonic generation in an asymmetric plasmonic slot waveguide. Opt Express 2014;22:18612–24.
[123] Sederberg S, Elezzabi AY. Integration of silicon-loaded nanoplasmonic waveguides onto a micro-machined characterization beam for nonlinear optics applications. Opt Mater 2015;48:150–5.
[124] Sederberg S, Elezzabi AY. Coherent visible-light-generation enhancement in silicon-based nanoplasmonic waveguides via third-harmonic conversion. Phys Rev Lett 2015;114:227401.
[125] MacDonald KF, Samson ZL, Stockman MI, Zheludev NI. Ultrafast active plasmonics. Nature Photon 2008;3:55–8.
[126] Verhagen E, Kuipers L, Polman A. Enhanced nonlinear optical effects with a tapered plasmonic waveguide. Nano Lett 2007;7:334–7.
[127] Caspers JN, Rotenberg N, van Driel HM. Ultrafast silicon-based active plasmonics at telecom wavelengths. Opt Express 2010;18:19761–9.
[128] Elezzabi AY, Han Z, Sederberg S, Van V. Ultrafast all-optical modulation in silicon-based nanoplasmonic devices. Opt Express 2009;17:11045–56.
[129] Sederberg S, Driedger D, Nielsen M, Elezzabi AY. Ultrafast all-optical switching in a silicon-based plasmonic nanoring resonator. Opt Express 2011;19:23494–503.
[130] Nielsen MP, Elezzabi AY. Ultrafast all-optical modulation in a silicon nanoplasmonic resonator. Opt Express 2013;21:20274–9.
[131] Zhu S, Lo GQ, Kwong DL. Electro-absorption modulation in horizontal metal-insulator-metal nanoplasmonic slot waveguides. Appl Phys Lett 2011;99:151114.
[132] Zhu S, Lo GQ, Kwong DL. Phase modulation in horizontal metal-insulator-silicon-insulator-metal plasmonic waveguides. Opt Express 2013;21:8320–30.
[133] Diaz FJ, Hatakeyama T, Rho J, et al. Sensitive method for measuring third order nonlinearities in compact dielectric and hybrid plasmonic waveguides. Opt Express 2016;24:545–54.
[134] Cai W, White JS, Brongersma ML. Compact, high-speed and power-efficient electrooptic plasmonic modulators. Nano Lett 2009;9:4403–11.
[135] Zhu S, Lo GQ, Kwong DL. Theoretical investigation of silicon MOS-type plasmonic slot waveguide based MZI modulators. Opt Express 2010;18:27802–19.
[136] Krasavin AV, Zayats AV. Electro-optic switching element for dielectric-loaded surface plasmon polariton waveguides. Appl Phys Lett 2010;97:041107.
[137] Zhu S, Lo GQ, Kwong DL. Theoretical investigation of ultra-compact and athermal Si electro-optic modulator based on Cu-TiO_2-Si hybrid plasmonic donut resonator. Opt Express 2013;21:12699–712.
[138] Taheri AN, Kaatuzian H. Numerical investigation of a nano-scale electro-plamonic switch based on metal-insulator-metal stub filter. Opt Quantum Electron 2015;47:159–68.
[139] Haffner C, Heni W, Fedoryshyn Y, et al. All-plasmonic Mach-Zehnder modulator enabling optical high-speed communication at the microscale. Nature Photon 2015;9:525–8.
[140] Irvine SE, Elezzabi AY. Ponderomotive acceleration using surface plasmon waves excited with femtosecond laser pulses. Appl Phys Lett 2005;86:264102.
[141] Esarey E, Sprangle P, Krall J. Laser acceleration of electrons in vacuum. Phys Rev E 1995;52:5443–53.
[142] Malka G, Lefebvre E, Miquel JL. Experimental observation of electrons accelerated in vacuum to relativistic energies by a high-intensity laser. Phys Rev Lett 1997;78:3314–17.
[143] Moore CI, Ting A, McNaught SJ, Qiu J, Burris HR, Sprangle P. A laser-accelerator injector based on laser ionization and ponderomotive acceleration of electrons. Phys Rev Lett 1999;82:1688–91.
[144] Irvine SE, Dechant A, Elezzabi AY. Generation of 0.4-keV femtosecond electron pulses using impulsively excited surface plasmons. Phys Rev Lett 2004;93:184801.
[145] Dombi P, Hörl A, Rácz P, et al. Ultrafast strong-field photoemission from plasmonic nanoparticles. Nano Lett 2013;13:674–8.

[146] Nagel PM, Robinson JS, Harteneck BD, et al. Surface plasmon assisted electron acceleration in photoemission from gold nanopillars. Chem Phys 2013;414:106–11.
[147] Greig SR, Elezzabi AY. An ultrafast silicon nanoplasmonic ballistic triode. Appl Phys Lett 2014;105:24115.
[148] Sederberg S, Elezzabi AY. Ponderomotive electron acceleration in a silicon-based nanoplasmonic waveguide. Phys Rev Lett 2014;113:167401.
[149] Paulus GG, Grasbon F, Walther H, et al. Absolute-phase phenomena in photoionization with few-cycle laser pulses. Nature 2001;414:182–84.
[150] Wittmann T, Horvath B, Helml W, et al. Single-shot carrier-envelope phase measurement of few-cycle laser pulses.Nat Phys 2009;5:357–62.
[151] Keiber S, Sederberg S, Schwarz A, et al. Electro-optic sampling of near-infrared waveforms. Nature Photon 2016;10:159–62.